



Signals Processing

Systems

Mekelweg 4,
2628 CD Delft

The Netherlands

<https://sps.ewi.tudelft.nl/>

SPS-2023-08

M.Sc. Thesis

Coded Excitation for Doppler Ultrasound Imaging of The Brain

Lixiang Zhu

Abstract

Doppler ultrasound imaging of cerebral blood flow faces challenges arising from a low signal-to-noise ratio (SNR) and a wide dynamic range. Echo signals received from blood cells are significantly weaker compared to surrounding tissues, such as the skull or brain soft tissue, resulting in inhibited visualization of small blood vessels and deep brain areas. To address this issue, this thesis explored the feasibility of employing and improving coded excitation techniques to enhance the SNR of Doppler ultrasound images. Furthermore, an optimized code for Doppler ultrasound imaging is designed, represented by a generalized encoding matrix. The research begins with the definition of a linear signal model that incorporates the encoding matrix. Subsequently, a trace-constraint optimization problem is formulated based on maximizing the Fisher information matrix to find the optimized encoding matrix. The feasibility and performance of the optimized encoding matrix are assessed through simulations on both small and large array settings, which operate above Nyquist sampling frequency and under Nyquist sampling frequency respectively. The imaging results indicate that the optimized code exhibits higher SNR in deep image regions compared to existing coded excitation methods like Barker code while using the same number of transmissions, bit length, and same average transmit energy, albeit with a trade-off of decreased axial resolution. Nonetheless, this resolution degradation can be mitigated through the application of the iterative imaging technique LSQR. Finally, the optimized code is tested in a clinical transducer setting, and a blood flow simulation is conducted. The outcomes showcase the capacity of the proposed optimized code to enable higher SNR in Doppler ultrasound imaging and more accurate and informative clinical assessments.

Coded Excitation for Doppler Ultrasound Imaging of The Brain

THESIS

submitted in partial fulfillment of the
requirements for the degree of

MASTER OF SCIENCE

in

ELECTRICAL ENGINEERING

by

Lixiang Zhu
born in Foshan, China

This work was performed in:

Signals Processing Systems Group
Department of Microelectronics
Faculty of Electrical Engineering, Mathematics and Computer Science
Delft University of Technology



Delft University of Technology

Copyright © 2023 Signals Processing Systems Group
All rights reserved.

DELFT UNIVERSITY OF TECHNOLOGY
DEPARTMENT OF
MICROELECTRONICS

The undersigned hereby certify that they have read and recommend to the Faculty of Electrical Engineering, Mathematics and Computer Science for acceptance a thesis entitled “**Coded Excitation for Doppler Ultrasound Imaging of The Brain**” by **Lixiang Zhu** in partial fulfillment of the requirements for the degree of **Master of Science**.

Dated: 25-08-2023

Chairman:

prof.dr.ir. G.J.T. Leus

Advisor:

dr.ir P.Kruizinga

Committee Members:

dr.ir.M.A.P. Pertijs

Abstract

Doppler ultrasound imaging of cerebral blood flow faces challenges arising from a low signal-to-noise ratio (SNR) and a wide dynamic range. Echo signals received from blood cells are significantly weaker compared to surrounding tissues, such as the skull or brain soft tissue, resulting in inhibited visualization of small blood vessels and deep brain areas. To address this issue, this thesis explored the feasibility of employing and improving coded excitation techniques to enhance the SNR of Doppler ultrasound images. Furthermore, an optimized code for Doppler ultrasound imaging is designed, represented by a generalized encoding matrix. The research begins with the definition of a linear signal model that incorporates the encoding matrix. Subsequently, a trace-constraint optimization problem is formulated based on maximizing the Fisher information matrix to find the optimized encoding matrix. The feasibility and performance of the optimized encoding matrix are assessed through simulations on both small and large array settings, which operate above Nyquist sampling frequency and under Nyquist sampling frequency respectively. The imaging results indicate that the optimized code exhibits higher SNR in deep image regions compared to existing coded excitation methods like Barker code while using the same number of transmissions, bit length, and same average transmit energy, albeit with a trade-off of decreased axial resolution. Nonetheless, this resolution degradation can be mitigated through the application of the iterative imaging technique LSQR. Finally, the optimized code is tested in a clinical transducer setting, and a blood flow simulation is conducted. The outcomes showcase the capacity of the proposed optimized code to enable higher SNR in Doppler ultrasound imaging and more accurate and informative clinical assessments.

Acknowledgments

As I am sitting down and writing this acknowledgment, I realized that exactly two years ago, I got on a flight from Guangzhou to Amsterdam, starting a new chapter of my life in the Netherlands as a master's student at TU Delft. Looking back at these two years, there was sweetness and bitterness. The thrill of passing all the exams. The exhaustion from after a long day staying in EWI trying to figure out a problem. All of these come to an end with the completion of this thesis. It was hard but fulfilling, and I will always cherish all the hardships and achievements in this process, and most importantly, all the people who have helped and encouraged me through this journey.

I would like to first give a big thanks to my daily supervisor Pieter Kruizinga from Erasmus MC. I first knew Pieter from a guest lecture during the Array Processing course in my first year. His broad knowledge of medical ultrasound imaging and the intriguing way he explained it was one of the main reasons I joined CUBE and did my internship there. Pieter's hard work and passion for the project were definitely a great source of inspiration for me during my internship and thesis. I learned a lot from him not only in the ultrasound field but also the quality of an independent researcher and the way to solve problems. I also want to thank all the other members of the CUBE. It was fun working with you guys and more fun during all the coffee breaks we had. I would not have been able to finish this thesis smoothly without your help and support.

I would also like to thank my supervisor prof. Geert Leus at TU Delft. I have always known Geert as a serious professor from all the lectures I had from him. During my thesis, he was always helpful and never hesitate to share his knowledge and ideas. I am really grateful for his straightforwardness and profound insights into my work, which helps me improve a lot. I learned how to become a rigorous researcher from him.

And to all my fellow students from the Signals Processing Systems group, it was a fun two years to study and work on the same course projects together. Without you guys, my life here would be much less fun.

Finally to my family. My dad, mom, and my little sister, support me unconditionally through this journey. Without you guys, I might not even be here to finish my master degree. I will always be grateful for giving me the opportunity to study and live in another country. And to all my dearest friends, thanks for making this journey more than enjoyable for me. Very special thanks to my boyfriend Kenneth for making me feel at home in a foreign country and being there for me through all my difficult times here.

Lixiang Zhu
Delft, The Netherlands
25-08-2023

Contents

Abstract	v
Acknowledgments	vii
1 Introduction	1
1.1 Problem Statements	2
1.2 Thesis Outline	3
1.3 Doppler Ultrasound Imaging	3
1.4 Coded Excitation Methods	6
1.5 Encoding Matrix	10
2 Mathematics Model and Imaging Techniques	13
2.1 Signal Model	13
2.2 Imaging Techniques	16
3 Optimization of Encoding Matrix	19
3.1 Encoding Matrix Optimization for Single Transmission	20
3.1.1 Optimal Solution	20
3.1.2 Suboptimal Solution	21
3.2 Encoding Matrix Optimization for Multiple Transmissions	22
3.3 Constraints in the Problem	24
4 Simulation Results	25
4.1 Small Array	25
4.2 Large Array	31
4.3 Clinical Transducer Results	34
4.3.1 B-mode results	34
4.3.2 Doppler Flow Simulations	42
5 Discussions and Future Work	47
5.1 Future Work	49
6 Conclusions	51

List of Figures

1.1	Two different methods of ultrasound imaging. (a) is the conventional ultrasound imaging method using line by line focused ultrasonic waves. (b) is the demonstration of a planewave imaging scheme.[1]	4
1.2	Data processing chain for Doppler ultrasound imaging using coded excitation schemes.	5
1.3	(a) and (b) show the Fourier spectra of the received ultrasound signal the signal after high-pass filtering for a pixel respectively. Both spectrum amplitudes are shown with the same normalization. It can be clearly seen that after high-pass filtering a large amount of energy is filtered out, resulting in diminished sensitivity in Doppler images. [2]	7
1.4	Illustration of Barker codes and Golay codes and the output after pulse compression.	8
1.5	Illustration of encoding matrix for different coded excitation methods. .	9
1.6	Comparison of ultrafast Doppler imaging on a mouse brain between (a) single pulse, (b) 13-bit Barker codes and (c) 8-bit Golay pairs. The first column shows the full image from the mouse brain, the second and third columns are the zoomed in area 1 around 5 <i>mm</i> (in black rectangular) and area 2 around 9 <i>mm</i> (in white rectangular) respectively. The dynamic range was then set between -35 dB to 0 dB to fully visualize the background noise dynamic.	11
2.1	Illustration of the model-based imaging problem.	16
3.1	Eigenvalues of matrix $\mathbf{Re}[\mathbf{A}_{tr}]$	23
4.1	Experiment setup in K-Wave for a small array with 128 elements and 25 μm pitch. The imaging area is a set of equidistantly placed point scatters.	26
4.2	Transmit pulse shape for (a) single short pulse (base pulse), (b) frequency spectrum of base pulse, (c) 5-bit Barker codes, (d) 5-bit random codes on elements 70 th and 80 th, and (e) 5-bit optimized codes on elements 70 th and 80 th.	27
4.3	The ten optimized encoding matrices for the small array. The size of the matrices is 128 \times 5. The y-axis indicates the channels and the x-axis indicates the bit length. The color map shows the amplitude and bi-phase encoding value of the code.	28
4.4	(a) shows the pressure field from 10 leading eigenvectors transmissions and (b) shows their corresponding imaging results.	29
4.5	Imaging results comparisons between optimized transmissions, Barker codes transmissions, planewave transmissions, and random transmissions (On the figure from left to right). The same level of noise where $SNR = 10dB$ is added to each scenario.	30

4.6	(a) shows the CRB over compounding eigenvectors for a pixel at depth 4.5 mm and depth 11 mm. (b) shows the CRB over depth for random, Barker, planewave, and optimized code. The results are after ten transmissions compounding.	30
4.7	Autocorrelation function for optimized codes (on the 80th element) and Barker code of length 5.	31
4.8	(a) shows the pressure field from 10 leading eigenvectors transmissions and (b) shows their corresponding imaging results for the large array with a transmitting center frequency of 15 MHz.	32
4.9	Beam steering and focusing ability demonstration for different frequency excitation pulse. (a) shows the pressure field for a 5 MHz excitation pulse when focusing at a point on the left, middle, and right side of the imaging area respectively from left to right. (b) shows the results for a 15 MHz excitation pulse.	33
4.10	The ten encoding matrices of the M5Sc-D phased array transducer. The encoding matrices have a size of 80×3 . The y-axis indicates the channels and the x-axis indicates the bit length. The color map shows the amplitude and bi-phase encoding value of the code.	35
4.11	Imaging results comparisons between optimized transmissions, Barker codes transmissions, planewave transmissions, and random transmissions (On the figure from left to right) in GE probe setting. The same level of noise where $SNR = 10dB$ is added to each scenario.	36
4.12	The SNR boxplot analysis for point scatters images with (From left to right) optimized codes, barker codes, single pulse planewave, and random codes. In each box, the bottom and top edges of the box represent the 25th and 75th percentiles in the data, and the red line inside the box marks the median. The whiskers represent the highest and lowest values in the data.	37
4.13	Imaging results from 3-bit, 5-bit, and 10-bit (from left to right) optimized codes. As the bit-length increases, the SNR of the image, especially in the deeper area is increased. The trade-off is a worsened resolution.	38
4.14	Autocorrelation function for 3-bit, 5-bit, and 10-bit optimized codes.	38
4.15	The SNR boxplot analysis for point scatters images with (From left to right) 3-bit, 5-bit, and 10-bit optimized codes. In each box, the bottom and top edges of the box represent the 25th and 75th percentiles in the data, and the red line inside the box marks the median. The whiskers represent the highest and lowest values in the data.	39
4.16	Optimized code imaging results using LSQR algorithm. Here we show the images after 1 to 40 iterations.	40
4.17	Normalized residual curves for Barker code and optimized code when adding iteration in LSQR.	41
4.18	Barker code imaging results using LSQR algorithm. Here we show the images after 1 to 40 iterations.	41

4.19	Image contrast to noise comparison between optimized code after 10 iterations and Barker code after 4 iterations. A vertical line from the image located at 0.24 <i>mm</i> is taken and plotted.	42
4.20	Numerical analysis of the performance of Barker code and optimized code. (a) shows the bar graph of the signal-to-noise ratio between Barker code and optimized code and (b) shows the bar graph of the contrast-to-noise ratio between Barker code and optimized code. They are calculated using the ROI shown in Figure 4.22, where the black rectangular indicated the blood vessel region and the white rectangular indicated the background region.	43
4.21	B-Mode images of the blood vessel from the optimized code and the Barker code.	43
4.22	(a) shows the Power Doppler images from 5-bit Barker code with noise-to-blood levels at 0, -15, and -30 dB (from left to right). (b) is the Power Doppler images from the optimized code. All the images are shown with the same colormap spectrum from 0 to -40 dB.	45

List of Tables

4.1	Autocorrelation function analysis for optimized codes (on the 80th element) and Barker code.	31
4.2	Autocorrelation function analysis for 3-bit, 5-bit, and 10-bit optimized code.	37

Ultrasonography, also known as ultrasound imaging, is nowadays one of the most important medical diagnostic methods. The first implementation of ultrasound in medical and diagnostic fields dates back to 1942 when Karl Dussik attempted to detect brain tumors by transmitting an ultrasound beam through the human skull. Later from 1948 to 1951, the invention of one-dimensional amplitude mode (A-mode) and two-dimensional brightness mode (B-mode) devices made the commercialization of ultrasonography becomes possible. The utilization of the Doppler effect promoted the development of Doppler ultrasound technology. Around the 1970s, the creation of spectral Doppler and color Doppler ultrasound instruments enabled the imaging of blood flow in the heart and brain. In clinical applications, a noninvasive way to detect blood flow velocity inside the brain is transcranial Doppler (TCD) ultrasound imaging [3] [4], which can assist in the diagnosis of diseases caused by blood clots such as strokes [5] [6] or sickle cell disease [4]. However, TCD suffers from a low signal-to-noise ratio (SNR) and a large dynamic range since the echo signals received from red blood cells are much weaker than that of the surrounding tissue, such as the skull or brain soft tissue. This disadvantage inhibits the visualization of small blood vessels and also deep brain areas, which can provide clinicians with important and more accurate diagnostic information [5]. Doppler ultrasound on small animals such as mice for neuroscience research is usually conducted after a craniotomy to avoid the high attenuation from the skull and achieve a high SNR and flow sensitivity.

Starting from the 1980s, with the maturity of ultrasound technology, researchers focused more on improving imaging quality. Two important criteria for imaging quality are SNR and frame rates. A high SNR can give a clearer image that helps with the diagnosis in clinical applications while higher frame rates can enable real-time imaging and improve the temporal resolution. There are mainly two ways to improve SNR, one is an invasive way which is by injecting microbubbles into subject bodies as contrast agents [7]. However, due to the short lifespan of microbubbles inside the body, this method tends to have low stability and consistency in imaging. The other is a noninvasive way, which is to increase the total amount of energy sent by the ultrasound transducer. This method has a low cost and is usually easy to implement in ultrasound systems. A few researchers have already explored this area.

Tiran and Deffieux et al. [8] designed a multiplane wave scheme to increase the SNR in Doppler ultrasound imaging. Instead of sending out one planewave each time like Mace et al. in [2], they proposed to transmit N wavefronts with different angles quasi simultaneously. It is reported that for N multiplane wave transmissions, the SNR can be increased by a factor of N compared to conventional Doppler ultrasound imaging. Researchers have also explored the use of coded excitation in ultrasound imaging. Misaridis and Jensen demonstrated in 2005 [9] [10] [11] that sending out longer encoded pulses, known as coded excitation, can increase the SNR of ultrasound

images as well as the penetration depth. Moreover, Zhao and Gao [12] showed that using long-bit streams of Barker code (a specific type of coded excitation) can significantly increase the sensitivity for ultrasound color flow imaging. Coded excitation involves using longer encoded pulses, achieved through appropriate coding of the transmit signal, allowing increased pulse duration without raising amplitude and avoiding tissue heating issues. It enables a drastic SNR increase in ultrasound imaging without exceeding the FDA safety limit [13], which refers to regulatory guidelines and limits set by the U.S. Food and Drug Administration (FDA) to ensure the safe and appropriate use of medical ultrasound devices. By decoding received echoes, axial resolution can be retrieved, albeit with a slight degradation. Building on the success of coded excitation in ultrasound imaging for over two decades and its long-standing use in radar for more than 70 years, researchers are now keen on exploring further improvements.

Coded excitation methods in ultrasound imaging can be enhanced through various approaches. One such avenue is the exploration of hybrid coding techniques, which involve combining different coding sequences to leverage their respective advantages. Fan and Rudlin [14] proposed a novel approach by convolving Barker and Golay codes, demonstrating that the combination of these codes effectively suppresses sidelobe levels and leads to an increase in SNR. Similarly, Benane and Bujoreanu et al. [15] introduced chirp-modulated Golay codes, integrating orthogonal binary codes with pre-enhanced chirp, resulting in a significant enhancement of more than 10 dB in the echo SNR.

Another avenue for improvement is the incorporation of advanced signal processing algorithms to decode and reconstruct received echoes efficiently. Vienneau and Byram [16] proposed using a Finite Impulse Response (FIR) filter to decode echoes from Barker code transmissions and effectively suppress sidelobe energy. Their method also allowed the design of longer Barker codes using Kronecker products, enabling transcranial functional ultrasound neuroimaging.

Furthermore, there exists potential for optimized code design to improve the SNR for Doppler ultrasound imaging. There has been extensive research in optimized code design in the radar area for robustness and high resolution [17] [18] and has shown great improvement in radar detectability. Although substantial research has been conducted on hybrid coding and advanced signal processing, there remains a gap in the literature regarding optimized code design for Doppler ultrasound imaging. Therefore, an intriguing avenue for investigation lies in the exploration of coding sequences that maximize SNR while achieving the desired penetration depth, potentially leading to significant improvements in Doppler ultrasound imaging performance.

1.1 Problem Statements

The primary objective of this thesis is to investigate and design optimized transmit codes for Doppler ultrasound imaging, focusing on increasing SNR. By addressing this problem, this study aims to improve conventional coded excitation schemes and contribute to the gap in optimized code design in ultrasound studies.

1.2 Thesis Outline

The first chapter will cover the background and motivation of this thesis, including basic Doppler ultrasound and coded excitation theories. In this chapter, the concept of encoding matrix will also be presented. The signal model and its corresponding imaging techniques will be discussed in Chapter 2, after which Chapter 3 will focus on articulating the optimization methods for the encoding matrix. Results are presented in Chapter 4, where the application scenario for the proposed method and its limitations are further discussed.

1.3 Doppler Ultrasound Imaging

Doppler ultrasound imaging is a well-established technique widely used for imaging blood vessels, leveraging the principles of ultrasound and the interaction of mechanical pressure waves with tissues and red blood cells. The Doppler-shifted ultrasound signals arise from the scattering of red blood cells, and the recorded Doppler frequency is directly related to the velocity of these cells. The Doppler frequency f_D can be expressed as [2]:

$$f_D = -\frac{2v}{c_0} f_{us} \cos \theta = f_R - f_T, \quad (1.1)$$

where v is the velocity of the scattering entity (e.g., red blood cells), c_0 is the speed of sound in the medium, f_{us} is the transmitted ultrasound frequency, and θ is the angle between the ultrasound beam and the direction of blood flow. A negative f_D indicates that the scatterer is moving away from the transducer (resulting in a lower received frequency f_R compared to the transmitted frequency f_T), while a positive f_D indicates movement towards the transducer (resulting in a higher f_R).

The core component of ultrasound imaging is the transducer, which consists of an array of piezoelectric elements capable of both transmitting and receiving mechanical pressure waves. When a voltage is applied to a piezoelectric element, it undergoes vibration, generating a mechanical pressure wave with a specific frequency. The frequency of vibration determines the ultrasound frequency used for imaging, typically ranging from 1 to 30 MHz.

During imaging, the transmitted pressure wave encounters various acoustic impedance as it penetrates tissues. The impedance differences cause echoes to backscatter back to piezoelectric elements. The elements then convert these echoes into small voltage signals, which is also known as radio frequency (RF) data. The ultrasound system records these RF data, which undergoes further processing, including high-pass filtering and beamforming, to create an image.

Conventional ultrasound imaging employs focused ultrasonic waves, as illustrated in Figure 1.1 (a). This approach involves sending a single focused wave during each transmission, reconstructing one line of the image at a time. However, this scanning method might not achieve enough sampling frequency and could result in not accurate analysis for functional ultrasound [2].

In contrast, planewave imaging utilizes one pulsed plane wave per transmission and captures backscattered echoes from all points within the image, as shown in Figure 1.1 (b). This enables the reconstruction of a full image from a single transmission using parallel beamforming, such as delay-and-sum beamforming. Planewave imaging offers several advantages over the conventional method. It can obtain a much higher number of images for the same number of firings and acquisition time. With a small number of planewave transmissions, it is possible to gain higher contrast, SNR, and resolution compared to the traditional ultrasound imaging method. Therefore, planewave imaging is particularly advantageous for Doppler imaging, where simultaneous excitation of all transducer elements is often preferred [2].

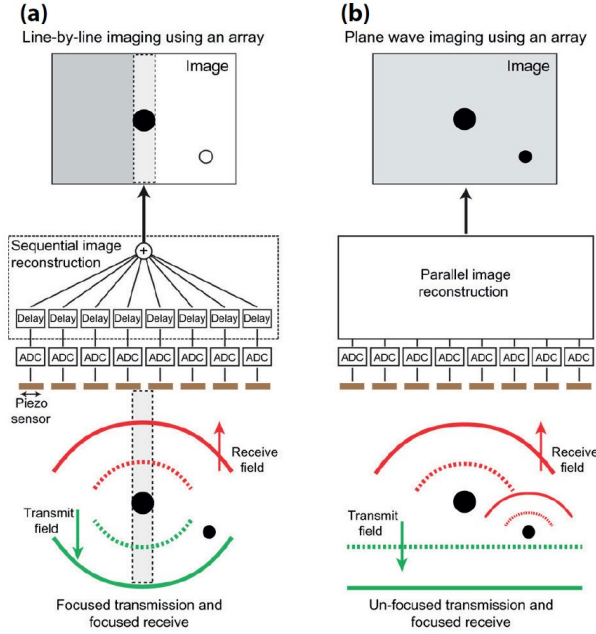


Figure 1.1: Two different methods of ultrasound imaging. (a) is the conventional ultrasound imaging method using line by line focused ultrasonic waves. (b) is the demonstration of a planewave imaging scheme.[1]

However, one of the trade-offs associated with planewave transmission, in comparison to conventional transmission, is a reduction in resolution and contrast. To mitigate this reduction, a technique known as compounding is commonly employed. Compounding involves consecutively sending out multiple planewaves with different angles to acquire information from various perspectives and then averaging the collected data points for each pixel. By compounding data obtained from these different angles, a high-resolution, high-contrast ultrasound compounded frame can be generated.

The number of transmissions L required to generate a compounded image depends on the highest Doppler frequency f_D that needs to be detected. While utilizing more transmissions enhances resolution, the maximal firing rate is related to imaging depth. An excessively high firing rate could potentially lead to transducer overheating and subsequent damage. Therefore, a balance must be struck between the number of transmissions and the desired resolution, taking into account practical considerations such

as imaging depth and the duty cycle of the transducer [2].

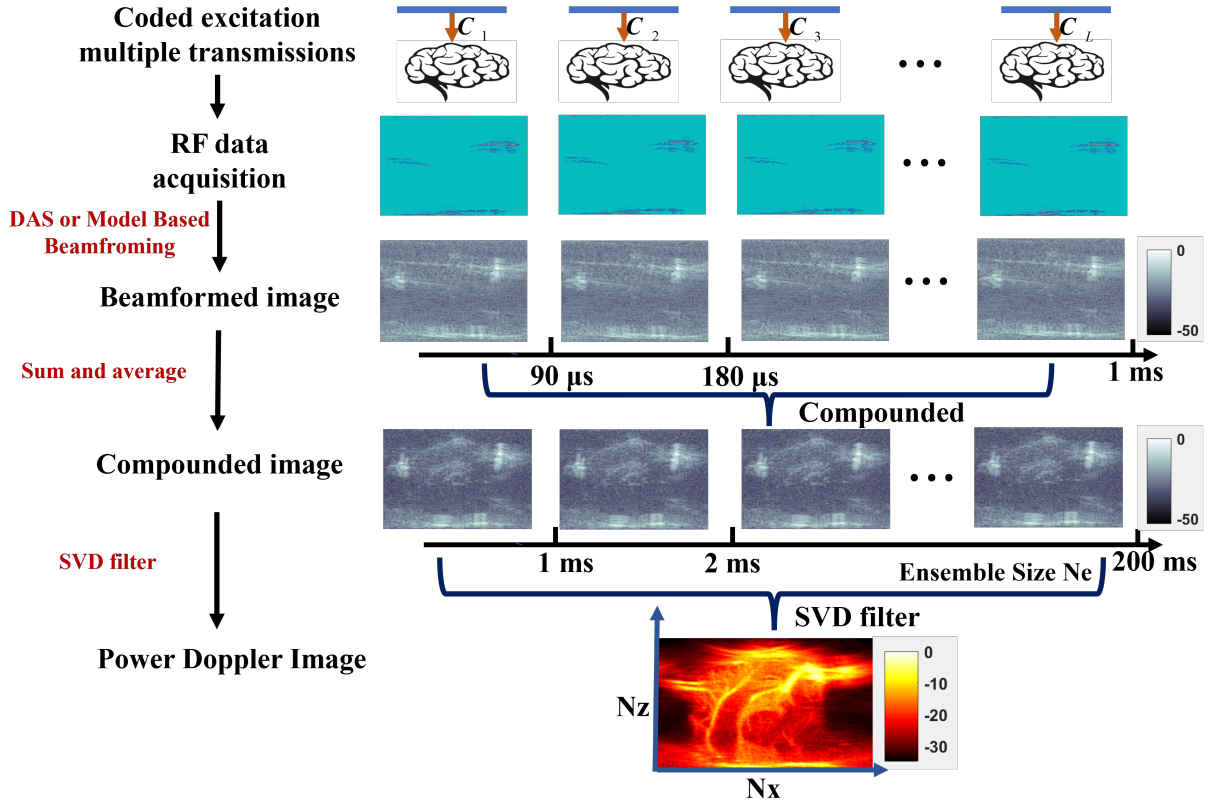


Figure 1.2: Data processing chain for Doppler ultrasound imaging using coded excitation schemes.

In this thesis, the performance of various coded excitation methods is assessed by examining the Power Doppler Image (PDI) they produce. Power Doppler is an imaging technique that concentrates on visualizing blood flow based on the amplitude or power of the Doppler signal, rather than its frequency shift. Unlike color Doppler imaging (CDI), which represents blood flow velocity through color mapping, PDI emphasizes the detection of moving blood cells by highlighting regions with strong Doppler signals, signifying the presence of blood flow regardless of its velocity. This approach proves especially valuable for capturing low-velocity or weak blood flow instances, such as in cases of slow or microvascular circulation, where CDI might struggle to offer clear representations [19].

The entire data processing chain, from raw RF data acquisition to PDI formation, is visualized in Figure 1.2, which provides an illustrative representation of the sequential steps involved in Doppler ultrasound imaging using coded excitation schemes. Detailed explanation for every step is unfolded as follows.

1. Raw RF Data Acquisition

Acquire raw RF data from L transmissions. The number of transmissions required typically ranges from 10 to 20 for mouse brain imaging. Montaldo et al.

experimentally validate that when L is larger than 16, the gain in SNR and image contrast will only have little improvement [20]. For Barker code or Golay code, this may involve L transmissions with the same transmitting pulse but different transmission angles. For random and other coded schemes, L distinct transmit pulses need to be used for the transmissions. It will be elaborated in later sections that all coded excitation schemes can be generalized into an encoding matrix \mathbf{C} , which can be seen from the first row in Figure 1.2. The L transmissions are completed in 1 ms.

2. Beamforming and Coherent Compounding

Beamformed on the obtained raw data to generate a single ultrasound image. This can be achieved through techniques like delay-and-sum beamforming, as described in [21], or Model-based beamforming, as discussed in [22]. Subsequently, coherently sum and average the L images to produce a single high resolution and higher SNR compounded frame. As can be seen in Figure 1.2, after compounding, the ultrasound image gained higher contrast (The compounded images at the fourth row).

3. Doppler processing and PDI formation

To visualize the blood flow characteristics, Ne compounded frames are sequentially acquired over time. This process culminates in a 2D space-time matrix with dimensions $(Nz \times Nx, Ne)$, where Nz , Nx , and Ne denote the number of samples in the spatial-depth, spatial-width (along the transducer array), and temporal dimensions, respectively. In Figure 1.2, $Ne = 200$, and this is also known as the ensemble size.

A Singular Value Decomposition (SVD) [23] filter can be applied to this 2D space-time matrix to separate the tissue and blood vessels. Another way to do it is by using a high-pass filter, which is computationally easier than SVD but has less accuracy [24]. The final PDI image is formed by taking an average over all the filtered temporal frames and reshaping back to an image with size $Nz \times Nx$.

Both the high pass filter and SVD filter will result in a significant energy loss. This can be seen from the energy level spectrum in Figure 1.2, where the beamformed image and compounded image have an energy spectrum from -50 to 0 dB while after the SVD filter only -30 to 0 dB left. Figure 1.3 also shows that after high-pass filtering, there is a large energy loss in the received signal. Consequently, utilizing coded excitation schemes can increase the received energy of the ultrasound signal and potentially improve the quality and sensitivity of Doppler imaging.

1.4 Coded Excitation Methods

Coded excitation is a specially designed longer encoded pulse that after pulse compression, yields a high mainlobe-to-sidelobe ratio, which results in comparable or slightly worse axial resolution compared to a single short pulse. The design of coded excitation

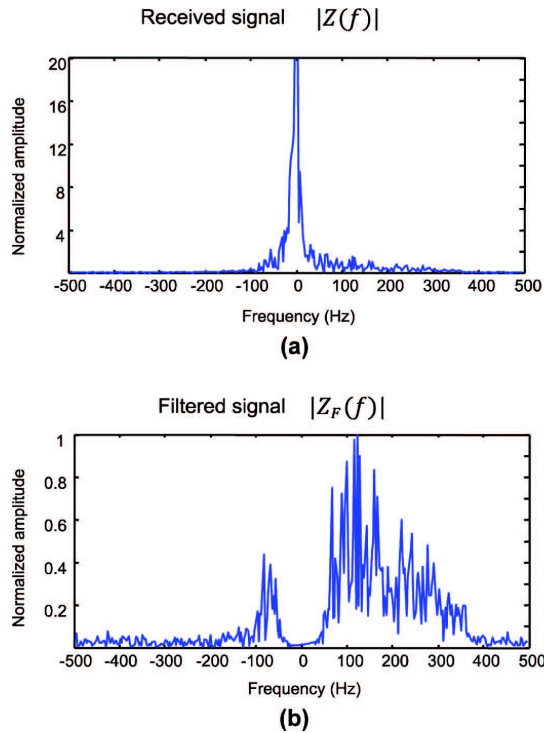


Figure 1.3: (a) and (b) show the Fourier spectra of the received ultrasound signal the signal after high-pass filtering for a pixel respectively. Both spectrum amplitudes are shown with the same normalization. It can be clearly seen that after high-pass filtering a large amount of energy is filtered out, resulting in diminished sensitivity in Doppler images. [2]

pulses typically employs frequency encoding or phase encoding techniques based on a short pulse [25].

Frequency encoding entails linearly modulating the carrier signal frequency, commonly achieved through linear frequency modulation (FM), also known as chirp. This technique is widely used in coded excitation schemes [10]. On the other hand, phase encoding is accomplished by modulating the phase of the transmitted pulse. Specifically, two commonly used phase encoding techniques are considered: linear phase modulation and bi-phase modulation [9]. In linear phase modulation, the phase of the transmitted pulse is modulated linearly. In bi-phase modulation, the transmitted pulse is encoded with either a 0-phase shift (represented by 1) or a 180-degree phase shift (represented by -1).

The two frequently used sequences for bi-phase modulation are the Golay code and Barker code. These codes exhibit specific properties that make them suitable for coded excitation schemes. Golay and Barker codes have been extensively employed in ultrasound imaging for their favorable autocorrelation properties and ability to produce high-quality images with improved signal-to-noise characteristics.

Barker Code

Barker code is a binary sequence that possesses good autocorrelation properties, which means that after matched filtering, the outputs have a high mainlobe-to-sidelobe ratio. An illustration of a 4-bit Barker code and the output of the matched filter can be seen in Figure 1.4.

However, existing Barker codes only have lengths of 2, 3, 4, 5, 7, 11, and 13, which limits the total amount of energy that can be transmitted. A way to generate longer codes is to calculate the Kronecker product of two Barker codes [16]. For example, the 4-bit Barker code [1 1 -1 1] can be lengthened to a 16-bit code [1 1 -1 1 1 1 -1 1 -1 -1 -1 1 1 -1 1] after doing a Kronecker product with itself. This, however, will result in a degradation in autocorrelation property. Further sidelobe suppression can be achieved by using an inverse filter [16] or spiking filter [25], but this will also result in a decrease in SNR. The expected gain in SNR using Barker codes is $\text{GSNR}_b = 10\log_{10}(K)$ [16], where K is the length of the Barker code.

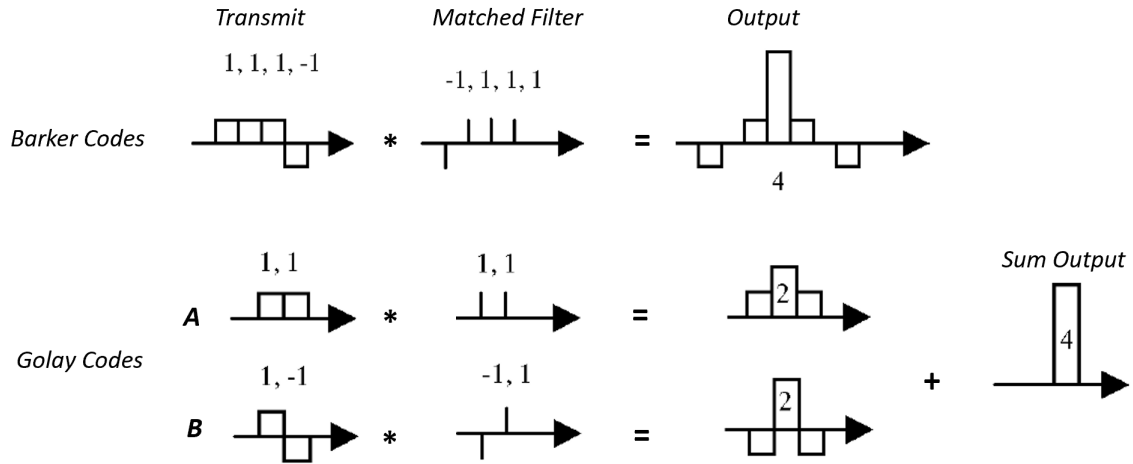


Figure 1.4: Illustration of Barker codes and Golay codes and the output after pulse compression.

Golay Code

The Golay code, also known as Golay complementary sequence pair, is defined as a pair of finite equal-length binary sequences. Different from single transmit signals like Barker codes that have range sidelobes after pulse compression, as can be seen from Figure 1.4, the Golay pair is designed to perfectly cancel out the range sidelobes. The condition that a pair of bidirectional sequences A and B of length K are Golay complementary sequences holds true if and only if the following formula holds,

$$A(k) * A(-k) + B(k) * B(-k) = 2K\delta(k), \quad (1.2)$$

where $*$ is the convolution operator. An illustration of a 2-bit Golay pair and the output of the matched filter can be seen in Figure 1.4. The expected SNR gain using

Golay codes is $\text{GSNR}_g = 10 \log_{10}(2K)$ [11].

The disadvantage of Golay pairs is that the frame rate will be halved since it requires two transmissions to get one image. This could also result in motion-dependent decoding errors. Trots et al. [26] proposed that by transmitting two pairs of mutually complementary orthogonal codes, the same frame rate as a single transmission code can be achieved.

Random Code

Barker encoding and Golay encoding methods solely utilize phase encoding over time. However, recent advancements by Ni et al. introduced a novel random encoding approach that incorporates both time and space encoding [27]. Unlike previous methods, where all transducer elements transmit the same encoded pulse, this new method excites each element with a distinct random encoded pulse. The authors demonstrated that the random transmitted waves constructively and destructively interfere in the imaging area, giving rise to intricate spatiotemporal interference patterns. Consequently, this generates low pixel-to-pixel correlations, resulting in a high-resolution image. The combination of time and space encoding in this random method opens up new possibilities for improving ultrasound imaging capabilities.

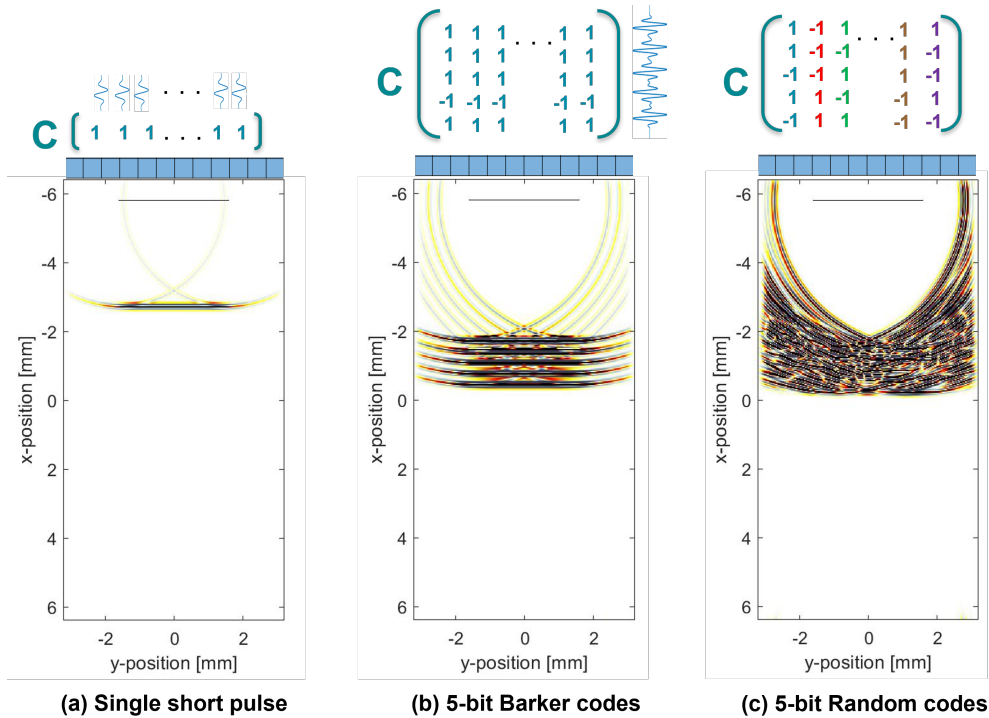


Figure 1.5: Illustration of encoding matrix for different coded excitation methods.

1.5 Encoding Matrix

Coded excitation techniques can be generalized using an encoding matrix denoted as $\mathbf{C} \in \mathbb{R}^{K \times N}$, where K represents the bit length of the code, and N corresponds to the number of elements on the transducer. In this study, amplitude encoding and bi-phase encoding are considered. Bi-phase encoding involves 0 degrees (indicating a positive sign) and 180 degrees (indicating a negative sign). The work by Richard et al. [28] discussed the advantages of amplitude encoding in radar applications, which has the potential to broaden the waveform bandwidth, thereby enhancing SNR and detection performance. Consequently, it becomes pertinent to investigate whether amplitude encoding could similarly improve the imaging SNR in ultrasound imaging within this study. Therefore, the value of each entry in matrix \mathbf{C} represents the weight for amplitude encoding and its polarity symbolizes the phase encoding for the transmitted ultrasound pulses. A visual representation of this encoding matrix concept is provided in Figure 1.5.

- For the non-encoded transmission scheme, the encoding matrix \mathbf{C} degenerates into an all-ones vector, resulting in uniform amplitude and phase weighting for each transducer element during transmission (Figure 1.5 (a)).
- For a Barker code transmission with a length of 5, \mathbf{C} is a matrix with all the columns as [1 1 1 -1 1] (Figure 1.5 (b)).
- In the case of random encoding, the entries in the encoding matrix \mathbf{C} are randomly selected from the set -1, 1 (Figure 1.5(c)).

In previous pilot experiments of mouse brain imaging conducted in CUBE, Erasmus MC, I have shown that coded excitation, in this case, Barker code and Golay code can indeed increase the SNR of images and detect more details in the deeper area, as can be seen in Figure 1.6.

It can be seen from the full image and the zoomed-in areas in Figure 1.6 that, with a single pulse transmission, the image has the most background noise in it and fewer blood vessels can be seen, especially in the deeper area (around 9 mm). The 13-bit Barker and 8-bit complementary Golay codes all show a much better image quality than the single pulse one. In the deep imaging area around 9 mm, as shown in the third column in Figure 1.6, Golay and Barker codes show the blood vessel while for the single pulse, the vessel is hardly visible. Golay codes show a slightly better result than the Barker code e.g., more blood vessels can be seen, shown in the zoomed-in area 1 in Figure 1.6. This is an expected result since the transmitted Golay pair is slightly longer than the Barker code.

This promising experimental result raises the question of whether we can design an optimized coded excitation scheme for Doppler ultrasound imaging, more specifically, an encoding matrix that outperforms traditional coded excitation methods.

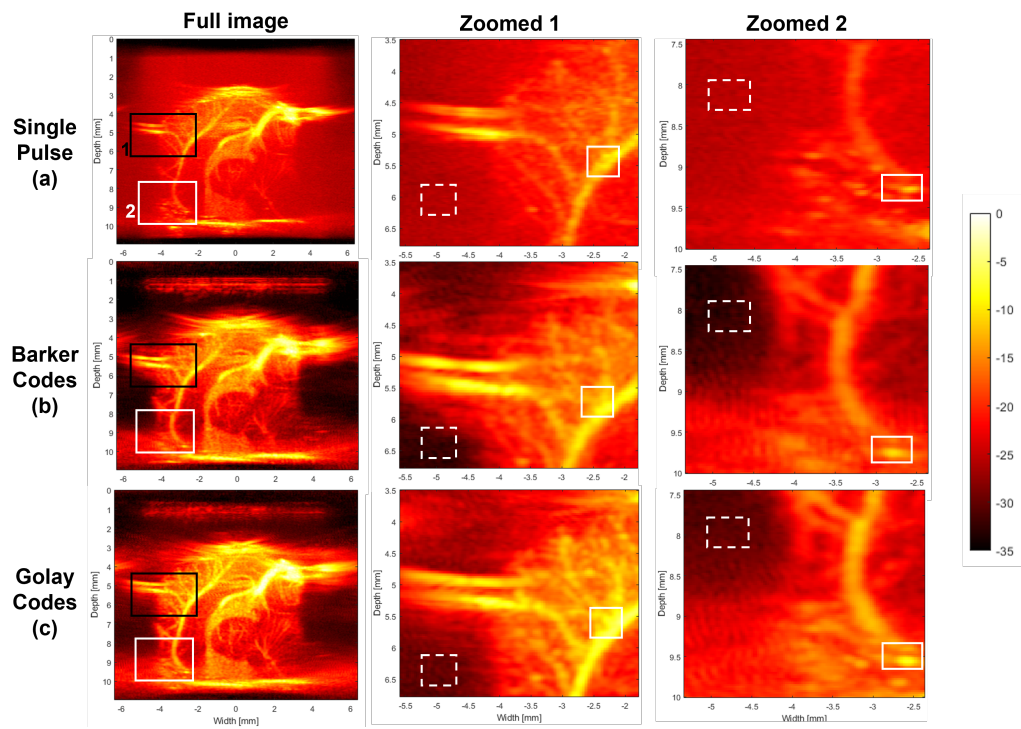


Figure 1.6: Comparison of ultrafast Doppler imaging on a mouse brain between (a) single pulse, (b) 13-bit Barker codes and (c) 8-bit Golay pairs. The first column shows the full image from the mouse brain, the second and third columns are the zoomed in area 1 around 5 *mm* (in black rectangular) and area 2 around 9 *mm* (in white rectangular) respectively. The dynamic range was then set between -35 dB to 0 dB to fully visualize the background noise dynamic.

This chapter focuses on building a comprehensive mathematical signal model for the ultrasound imaging problem. The integration of the encoding matrix \mathbf{C} into the model and its impact on image reconstruction will be explored. Furthermore, three main imaging techniques will be discussed to identify the most suitable approach for the specific problem addressed in this thesis.

2.1 Signal Model

The initial consideration in constructing a signal model is to determine the relevant information that needs to be incorporated. In medical ultrasound imaging, the conventional approach only takes the geometric information in the imaging area into account, which involves employing delay-and-sum (DAS) beamforming techniques. DAS beamforming leverages the time delay associated with a signal traveling from the transmitting element to the imaging point and back to the receiving element. By applying appropriate time delays to the received signals at each receiving element and subsequently summing them, an image is formed [21]. A limitation of DAS is that it assumes a propagation medium with a homogeneous speed of sound. Additionally, DAS does not work optimally when each element on the transducer transmits different pulses (e.g. random codes) since the interference between different pulses will result in incoherence summation and delay mismatch. Another shortage is that it does not accommodate the inclusion of the encoding matrix \mathbf{C} in the model.

To overcome these limitations, a more sophisticated technique known as model-based beamforming is adopted. This approach utilizes a signal model that accounts for various factors influencing ultrasound wave propagation, including tissue density, scattering, attenuation, and spherical spreading. By integrating this knowledge into the image reconstruction process, model-based beamforming can mitigate artifacts and enhance spatial resolution.

In the context of a transducer with N elements, consider a single transmit-receive event where all the elements transmit and subsequently receive the backscattered signal. The first step of model-based beamforming is to discretize the imaging area into a virtual grid comprising M pixels of equal size. Each pixel is treated as a potential scatterer and is assigned a reflection coefficient x_m , representing the property to be estimated for image reconstruction. Under the assumption of Born approximation [29] and linear transducer transfer function, a single-element measurement model can be expressed as a linear combination of the scattering coefficients and pulse-echo signals from all scatterers [22]. The Born approximation assumes that the interaction of an ultrasound wave with biological tissues is a linear process, where the scattered waves are directly proportional to the incident ultrasound wave, and is applicable when the

contrast between different tissue types is relatively small and significant nonlinear effects are not present during wave propagation.

In this thesis, all the models will be built in the frequency domain. Assume a sampled frequency set $\Omega = \{\omega_1, \omega_2, \dots, \omega_T\}$, where the frequencies are uniformly sampled within the positive side of pulse bandwidth, the linear measurement model for a single receiving element n at frequency ω can be expressed as

$$y_n[\omega] = \sum_{m=1}^M x_m h_r[\omega] g_{n,m}^{(r)}[\omega] \sum_{i=1}^N g_{m,i}^{(t)}[\omega] s_i[\omega] h_t[\omega]. \quad (2.1)$$

In this signal model, $y_n[\omega]$ represents the received ultrasound signal on the n th element and x_m denotes the scattering intensity of the m th pixel. $s_i[\omega]$ represents the excitation pulse sent by element i at frequency ω . The Green's function at frequency ω on pixel m measured at element n is denoted as $g_{n,m}^{(r)}[\omega]$. Furthermore, $g_{m,i}^{(t)}[\omega]$ is the Green's function for the wave propagating from the transmitting element i to pixel m . Here, the superscript (r) and (t) refer to the receive Green's function and the transmit Green's function.

In the context of this thesis, $h_t[\omega]$ and $h_r[\omega]$ correspond to the transmit and receive responses of the transducer, respectively. It is assumed that they are known in this research.

The computation of the Green's function takes into account factors such as the distance between the transmitting \receiving elements and each pixel, attenuation during propagation in the tissue, and the spreading factor. The functions $g_{m,i}^{(t)}[\omega]$ and $g_{n,m}^{(r)}[\omega]$ can be defined as follows,

$$g_{m,i}^{(t)}[\omega] = \exp\left(-j \frac{\omega}{c_0} d_{i,m}\right), \quad (2.2)$$

$$g_{n,m}^{(r)}[\omega] = \frac{1}{4\pi(d_{i,m} + d_{m,n})} \times \exp\left(-j \frac{\omega}{c_0} d_{m,n}\right). \quad (2.3)$$

Here, $d_{i,m}$ denotes the distance from the transmitting element i to pixel m , and $d_{m,n}$ is the distance traveled by the backscattered signal from pixel m to sensor n . c_0 corresponds to the speed of sound in the medium. The first term in equation (2.3) accounts for the geometric spreading of the pressure field, encompassing the entire distance the wave travels from the source to the pixel and back to the sensor. Typically, the Green's function is written in one expression, combining both transmit and receive terms. However, the geometric spreading term cannot be separated into two distinct components since the distances $d_{i,m}$ and $d_{m,n}$ are part of the same overall wave propagation path and are not independent of each other. As a result, the geometric spreading term is only considered in the receive Green's function. The exponential terms in both (2.2) and (2.3) represent the phase shift caused by the delay from the source to the pixel and back to the sensor.

Note that the excitation pulse $s_i[\omega]$ in equation (2.1) is transmit-element-dependent. Remember in section 1.5 we show that every transmission scheme, including single short pulse planewave transmissions and long coded excitation transmissions, can be generalized and numerically shown in an encoding matrix \mathbf{C} . In this thesis, a less

complicated case where all N elements transmit longer pulses consisting of an equal number K of base pulses and every base pulse is amplitude and bi-phase encoded with a weight $c_{n,k}$ is considered. Thus, the excitation pulse $s_i[\omega]$ at transmitting element i can be written as,

$$s_i[\omega] = \sum_{k=1}^K c_{i,k} \cdot p_k[\omega] = \mathbf{c}_i^T \mathbf{p}[\omega], \quad (2.4)$$

where $p_k[\omega]$ denotes the k th base pulse. The relation between two consecutive base pulse is $p_{k+1}[\omega] = p_k[\omega]e^{-j\omega\tau}$ where τ is the duration of one base pulse. $\mathbf{p}[\omega] = [p_1[\omega], p_2[\omega], \dots, p_K[\omega]]^T$ is the base pulse vector and $\mathbf{c}_i = [c_{i,1}, c_{i,2}, \dots, c_{i,K}]^T$ is the amplitude and bi-phase codes related to transmit element i .

Till now only the linear measurement model for one sensor element is considered. If we take all the sensor elements into account, the measurements from all elements are stacked in a vector $\mathbf{y}[\omega] \in \mathbb{C}^N$, and the transmit and receive Green's functions for every element and pixel pair can be stored in a matrix. The measurement model for all elements at frequency ω can be written as,

$$\mathbf{y}[\omega] = h_r[\omega]h_t[\omega]\mathbf{G}^{(r)}[\omega]\text{diag}(\mathbf{G}^{(t)}[\omega]\mathbf{C}\mathbf{p}[\omega])\mathbf{x}. \quad (2.5)$$

Here $\mathbf{C} \in \mathbb{R}^{N \times K}$ is the phase encoding matrix, defined as $\mathbf{C} = [\mathbf{c}_1, \mathbf{c}_2, \dots, \mathbf{c}_N]^T$. *diag* is an operator to transform a vector into a square diagonal matrix with the elements of the vector on its main diagonal. Vector $\mathbf{x} \in \mathbb{R}^M$ contains the scattering intensities from all pixels. $\mathbf{G}^{(r)}[\omega] \in \mathbb{C}^{N \times M}$ is the receive Green's function matrix at frequency bin ω and $\mathbf{G}^{(t)}[\omega] \in \mathbb{C}^{M \times N}$ is the transmit Green's function matrix. They are defined as follows,

$$\mathbf{G}^{(r)}[\omega] = \begin{bmatrix} g_{1,1}^{(r)}[\omega] & g_{1,2}^{(r)}[\omega] & \dots & g_{1,M}^{(r)}[\omega] \\ g_{2,1}^{(r)}[\omega] & g_{2,2}^{(r)}[\omega] & \dots & g_{2,M}^{(r)}[\omega] \\ \vdots & \vdots & \ddots & \vdots \\ g_{N,1}^{(r)}[\omega] & g_{N,2}^{(r)}[\omega] & \dots & g_{N,M}^{(r)}[\omega] \end{bmatrix}, \quad (2.6)$$

$$\mathbf{G}^{(t)}[\omega] = \begin{bmatrix} g_{1,1}^{(t)}[\omega] & g_{1,2}^{(t)}[\omega] & \dots & g_{1,N}^{(t)}[\omega] \\ g_{2,1}^{(t)}[\omega] & g_{2,2}^{(t)}[\omega] & \dots & g_{2,N}^{(t)}[\omega] \\ \vdots & \vdots & \ddots & \vdots \\ g_{M,1}^{(t)}[\omega] & g_{M,2}^{(t)}[\omega] & \dots & g_{M,N}^{(t)}[\omega] \end{bmatrix}. \quad (2.7)$$

It is clear from (2.5) that every element of the encoding matrix \mathbf{C} is linear with the other components in the equation. In the following, the frequency notation ω is dropped to keep the equation clear and concise. As a result, the right part of (2.5) can be written into $\mathbf{G}(\mathbf{C}) = \sum_{n=1}^N \sum_{k=1}^K c_{n,k} \mathbf{G}_{n,k}$, where $\mathbf{G}_{n,k} \in \mathbb{C}^{N \times M}$ is given by

$$\mathbf{G}_{n,k} = h_r h_t \mathbf{G}^{(r)} \text{diag}(\mathbf{G}^{(t)} \mathbf{O}_{n,k} \mathbf{p}). \quad (2.8)$$

$\mathbf{O}_{n,k} \in \mathbb{R}^{N \times K}$ is a matrix with only one non-zero entry, i.e., $[\mathbf{O}_{n,k}]_{n,k} = 1$. $\mathbf{O}_{n,k}$ plays the role of selecting which code entry is active.

Assume the measurement model contains additive noise. By calculating other frequency components of matrix $\mathbf{G}(\mathbf{C})$ following the same procedures above and stacking them and all frequency measurements vertically together, (2.5) can be written into the linear model,

$$\mathbf{y} = \mathbf{G}(\mathbf{C})\mathbf{x} + \mathbf{n}. \quad (2.9)$$

Where vector $\mathbf{y} \in \mathbb{R}^{TN}$ encompasses all measured samples from the array transducer in the frequency domain, where T represents the number of samples and N denotes the number of transducer elements. Matrix $\mathbf{G}(\mathbf{C}) \in \mathbb{R}^{TN \times M}$ is referred to as the model matrix, where each column corresponds to the impulse response that would be measured if only that pixel were active. It is important to note that (2.9) is valid only when multiple reflections between scatterers are not considered, which is under Born approximation. Figure 2.1 illustrates the process of building the general imaging model.

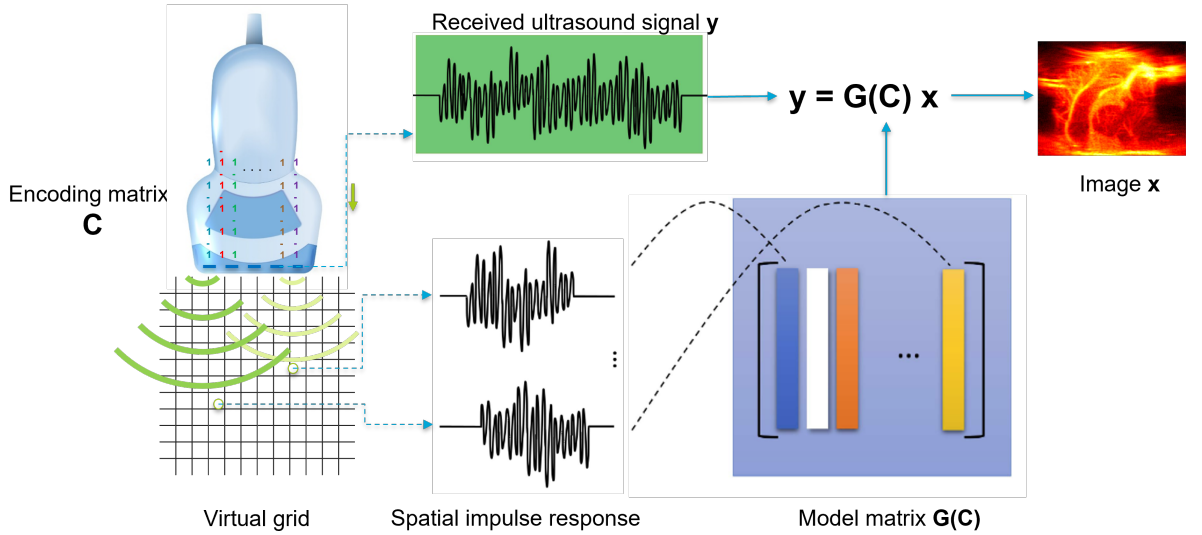


Figure 2.1: Illustration of the model-based imaging problem.

For a single short pulse planewave transmission, the encoding matrix \mathbf{C} degrades to an all-one vector, denoted by $\mathbf{1}^T$ and this special signal model can be written as,

$$\mathbf{y} = \mathbf{G}(\mathbf{1}^T)\mathbf{x} + \mathbf{n}. \quad (2.10)$$

The signal model (Equation (2.10)) remains linear with respect to vector \mathbf{x} , similar to the general imaging model (Equation (2.9)). As a result, both signal models can be solved using the same inversion techniques

2.2 Imaging Techniques

Assume the noise $\mathbf{n} \in \mathbb{C}^{NT}$ in signal model (2.9) is zero mean complex white Gaussian noise, $\mathbf{n} \sim \mathcal{CN}(0, \sigma_n^2 \mathbf{I})$. There are multiple imaging techniques to estimate image \mathbf{x}

from measurement \mathbf{y} . Since the model matrix $\mathbf{G}(\mathbf{C})$ contains spatial and temporal information about pixels in each column. When \mathbf{y} and the model matrix are combined to estimate the image, they utilize all the measurement data when estimating any single pixel, and this can be seen as a spatio-temporal estimator. A spatio-temporal estimator leverages the information from the neighboring locations and time stamps to improve the estimation accuracy and robustness [22]. In the following, a few imaging techniques that are related to this thesis will be discussed for the general signal model (2.9). For more detailed information regarding these imaging techniques, we refer the interested reader to [30].

Matched Filtering: This technique aims to maximize the signal-to-noise ratio (SNR) in the presence of additive Gaussian noise. It correlates the measurement data \mathbf{y} with the pre-defined model matrix, leading to the solution:

$$\hat{\mathbf{x}} = \mathbf{G}(\mathbf{C})^H \mathbf{y}. \quad (2.11)$$

Matched filtering is easy to implement since it only takes the conjugate transpose of the model matrix and measurement data into account. However, this method heavily relies on the accurate construction of the pre-defined model matrix.

Least Squares Estimation: This imaging technique involves minimizing the sum of squared differences between the measurement vector \mathbf{y} and the estimated vector $\mathbf{G}(\mathbf{C})\mathbf{x}$:

$$\hat{\mathbf{x}} = \arg \min_{\mathbf{x}} \|\mathbf{y} - \mathbf{G}(\mathbf{C})\mathbf{x}\|_2^2. \quad (2.12)$$

The least squares estimator can be solved by finding the pseudoinverse of the model matrix $\mathbf{G}(\mathbf{C})$,

$$\hat{\mathbf{x}} = \mathbf{G}(\mathbf{C})^\dagger \mathbf{y} = (\mathbf{G}(\mathbf{C})^H \mathbf{G}(\mathbf{C}))^{-1} \mathbf{G}(\mathbf{C})^H \mathbf{y}. \quad (2.13)$$

The last expression only holds when $\mathbf{G}(\mathbf{C})$ is full rank and its inversion exists. If the model matrix $\mathbf{G}(\mathbf{C})$ is ill-posed, in order to find feasible solutions, regularization techniques should be applied. The most commonly used technique is Tikhonov regularization [31], which requires to modify equation (2.13) to,

$$\hat{\mathbf{x}} = \arg \min_{\mathbf{x}} (\|\mathbf{y} - \mathbf{G}(\mathbf{C})\mathbf{x}\|_2^2 + \lambda \|\mathbf{x}\|_2^2). \quad (2.14)$$

The second term in equation (2.14) plays the regularization penalty part and provides prior knowledge about the estimated problem. The regularization term λ can be found at the corner of the L-curve. The L-curve is a graphical tool used in the context of regularization to find an appropriate value for the regularization parameter λ . The L-curve is created by plotting the norm of the residual error $\|\mathbf{y} - \mathbf{G}(\mathbf{C})\mathbf{x}\|_2$ (y-axis) against the norm of the regularized solution $\|\mathbf{x}\|_2$ (x-axis) for different values of the regularization parameter λ . The solution now becomes,

$$\hat{\mathbf{x}} = (\mathbf{G}(\mathbf{C})^H \mathbf{G}(\mathbf{C}) + \lambda \mathbf{I})^{-1} \mathbf{G}(\mathbf{C})^H \mathbf{y}. \quad (2.15)$$

This shows that regularization helps to make term $\mathbf{G}(\mathbf{C})^H \mathbf{G}(\mathbf{C})$ invertible by adding an identity matrix to it.

Minimum Mean Square Error Estimation (MMSE): Besides minimizing the sum of the squared modeling error, another way to approach this is by minimizing the mean square error, which can be written as,

$$\hat{\mathbf{x}} = \arg \min_{\mathbf{x}} \mathbb{E}((\mathbf{x} - \hat{\mathbf{x}})(\mathbf{x} - \hat{\mathbf{x}})^H). \quad (2.16)$$

If \mathbf{x} is random and has a prior distribution of $\mathcal{N}(\mu_{\mathbf{x}}, \mathbf{C}_{\mathbf{x}})$. For the linear model and under the zero-mean white noise assumption, $\hat{\mathbf{x}}$ is given by,

$$\hat{\mathbf{x}} = \mathbb{E}(\mathbf{x}|\mathbf{y}) = \mu_{\mathbf{x}} + (\mathbf{C}_{\mathbf{x}}^{-1} + \mathbf{G}(\mathbf{C})^H \mathbf{C}_{\mathbf{n}}^{-1} \mathbf{G}(\mathbf{C}))^{-1} \mathbf{G}(\mathbf{C})^H \mathbf{C}_{\mathbf{n}}^{-1} (\mathbf{y} - \mathbf{G}(\mathbf{C})\mu_{\mathbf{x}}). \quad (2.17)$$

The prior distribution of \mathbf{x} is often not known and needs an assumption. Note that (2.17) will be equal to the Tikhonov least squares estimation (2.15) when \mathbf{x} is zero mean with covariance matrix $\mathbf{C}_{\mathbf{x}} = \lambda \mathbf{I}$.

Among these imaging techniques, matched filtering (2.11) will be the main technique employed in this thesis due to its efficiency and ease of implementation, which is particularly advantageous considering the large imaging area in this thesis.

Optimization of Encoding Matrix

3

In the previous chapter, a general imaging model encompassing the encoding matrix was formulated, and various imaging techniques were discussed. This chapter focuses on finding the optimal encoding matrix in the mean-squared-error sense. It begins by demonstrating how the optimization problem can be translated into minimizing the mean square error of the estimator concerning the encoding matrix. Subsequently, a suboptimal but more flexible and efficient solution will be explored, followed by presenting the joint optimization scheme for Doppler ultrasound imaging.

The general signal model with additive zero-mean white complex Gaussian noise (2.9) was introduced in Section 2.1. The goal is to find an optimized encoding matrix \mathbf{C} that results in a high-quality image estimate $\hat{\mathbf{x}}$. For parameters estimation problems, a commonly used performance measurement is based on minimizing the trace of the error covariance matrix [32] [33]. In this thesis, the image estimation error covariance matrix is utilized to find an optimized encoding matrix, which is denoted as,

$$\mathbf{C}_e = \mathbb{E}((\mathbf{x} - \hat{\mathbf{x}})(\mathbf{x} - \hat{\mathbf{x}})^H). \quad (3.1)$$

However, the prior distribution of the image \mathbf{x} is not known in this case and (3.1) can not be found in a closed-form expression. Therefore, Cramér–Rao lower bound (CRB) is used as a simpler substitute for the error covariance matrix. CRB provides a lower limit on how well an unbiased estimator can perform in terms of its variance. It is derived from the Fisher Information, which quantifies how much information a dataset carries about the parameter of interest. The relationship between the error covariance of any estimator and its CRB can be found in [34],

$$\mathbb{E}((\mathbf{x} - \hat{\mathbf{x}})(\mathbf{x} - \hat{\mathbf{x}})^H) \geq \mathbf{CRB}(\mathbf{x}) = \mathbf{F}^{-1}(\mathbf{x}). \quad (3.2)$$

The Fisher information matrix $\mathbf{F}(\mathbf{x})$ for the linear Gaussian model (2.9) is calculated as [30],

$$\mathbf{F}(\mathbf{x}) = \sigma_n^{-2} \mathbf{G}(\mathbf{C})^H \mathbf{G}(\mathbf{C}), \quad (3.3)$$

which due to the linearity of the model becomes independent of the image \mathbf{x} and hence only depends on the matrix $\mathbf{G}(\mathbf{C})$. Therefore, minimizing the MSE can be written as minimizing,

$$f(\mathbf{C}) = \frac{1}{M} \text{trace}((\sigma_n^{-2} \mathbf{G}(\mathbf{C})^H \mathbf{G}(\mathbf{C}))^{-1}). \quad (3.4)$$

Importantly, this objective function $f(\mathbf{C})$ is independent of the unknown variable \mathbf{x} .

3.1 Encoding Matrix Optimization for Single Transmission

3.1.1 Optimal Solution

With the cost function (3.4) and the addition of an energy constraint, the optimization function can be formulated as follows,

$$\begin{aligned} \min \quad & f(\mathbf{C}) \\ \text{s.t.} \quad & \|\mathbf{c}\|^2 = 1, \end{aligned} \quad (3.5)$$

where $\mathbf{c} = \text{vec}(\mathbf{C})$. However, the cost function is not convex with respect to \mathbf{C} . The nonconvexity arises from the presence of quadratic forms in the cost function. For instance, notice that,

$$\begin{aligned} \mathbf{G}(\mathbf{C})^H \mathbf{G}(\mathbf{C}) &= \left(\sum_{i=1}^{NK} c_i \mathbf{G}_i \right)^H \left(\sum_{j=1}^{NK} c_j \mathbf{G}_j \right) \\ &= \sum_{i=1}^{NK} \sum_{j=1}^{NK} c_i^* c_j \mathbf{G}_i^H \mathbf{G}_j. \end{aligned} \quad (3.6)$$

c_i^* represents the complex conjugate of c_i . Solving nonconvex problems can be challenging because traditional optimization algorithms may get stuck in local optima or have difficulty converging. This necessitates some relaxation before solving this minimization problem. To make the optimization problem more tractable, a common relaxation technique is used, which involves absorbing the quadratic term $c_i^* c_j$ into a single variable $C_{i,j}^*$ [32]. This leads to a linear cost function with respect to the variable $C_{i,j}^*$,

$$\mathbf{G}(\mathbf{C})^H \mathbf{G}(\mathbf{C}) = \sum_{i=1}^{NK} \sum_{j=1}^{NK} C_{i,j}^* \mathbf{G}_i^H \mathbf{G}_j. \quad (3.7)$$

By storing all $C_{i,j}^*$ into a matrix \mathbf{C}^* , where $[\mathbf{C}^*]_{i,j} = C_{i,j}^*$. The equivalence between (3.6) and (3.7) only holds when $\mathbf{C}^* = \mathbf{c}\mathbf{c}^H$, which requires \mathbf{C}^* to be a rank 1 matrix and this constraint is not convex. One way to relax the constraint $\mathbf{C}^* - \mathbf{c}\mathbf{c}^H = 0$ is by writing the original function as [35],

$$\begin{aligned} \min \quad & f(\mathbf{C}^*) \\ \text{s.t.} \quad & \mathbf{C}^* \succeq 0 \\ & \mathbf{1}^T \text{diag}(\mathbf{C}^*) = 1. \end{aligned} \quad (3.8)$$

By solving for \mathbf{C}^* , the optimized encoding matrix can be found. However, since the solution $\hat{\mathbf{C}}^*$ from (3.8) is not guaranteed to be rank-1, approximating the rank-1 solution can be done by finding the largest eigenvector of $\hat{\mathbf{C}}^*$. Another widely used approach is the randomization method [36], where $\hat{\mathbf{C}}^*$ is treated as a covariance matrix. The randomization method involves generating multiple random vectors $\hat{\mathbf{c}} \sim \mathcal{N}(0, \hat{\mathbf{C}}^*)$, following a Gaussian distribution with zero mean and covariance $\hat{\mathbf{C}}^*$. Note that here every random realization is normalized to satisfy the energy constraint. Each candidate

is then applied to the original problem (3.5), and the realization with the lowest MSE is selected as the solution.

The randomization method can be interpreted as solving the nonconvex problem (3.5) on average over the distribution of $\hat{\mathbf{c}} \sim \mathcal{N}(0, \hat{\mathbf{C}}^*)$ [37].

3.1.2 Suboptimal Solution

The previous optimization scheme (3.8) represents the optimal MSE solution. However, due to the large number of pixels in the imaging area (over $M > 40000$), the cost function $f(\mathbf{C}^*)$ involves calculating and saving a significant number ($NK > 400$) of $\mathbf{G}_i^H \mathbf{G}_j \in \mathbb{C}^{M \times M}$ matrices, making it computationally challenging and memory-intensive to implement and solve in *cvx*, which is a toolbox in MATLAB for solving convex optimization problem [38]. To address this limitation, a suboptimal optimization function that is less complex and more efficient is explored.

Instead of minimizing the trace of MSE, we can maximize the trace of the Fisher information matrix. This approach provides more flexibility than (3.8). Unlike CRB, which is a global lower bound on the error covariance matrix \mathbf{C}_e for all components in vector \mathbf{x} , the Fisher information matrix can give insight into how much information a certain set of measurements contains about the parameter being estimated. Therefore, with a large number of pixels, a subset of the imaging area can be selected to build the model matrix and maximize the Fisher information in that specific ROI to obtain an optimized encoding matrix. This method proves to be more efficient and flexible compared to the optimization scheme in (3.8), although it may not be optimal in the MSE sense, leading to a potential deterioration in image quality.

The expression for the Fisher information matrix is given in equation (3.3). By transforming $\mathbf{G}(\mathbf{C})^H \mathbf{G}(\mathbf{C})$ using (3.6), it can be expressed as a Kronecker product:

$$\begin{aligned} \mathbf{G}(\mathbf{C})^H \mathbf{G}(\mathbf{C}) &= \sum_{i=1}^{NK} \sum_{j=1}^{NK} c_i^* c_j \mathbf{G}_i^H \mathbf{G}_j \\ &= \sum_{i=1}^{NK} \sum_{j=1}^{NK} c_i^* c_j \mathbf{A}_{i,j} \\ &= (\mathbf{c}^H \otimes \mathbf{I}) \mathbf{A} (\mathbf{c} \otimes \mathbf{I}), \end{aligned} \tag{3.9}$$

where \otimes is the Kronecker product, $\mathbf{A}_{i,j} = \mathbf{G}_i^H \mathbf{G}_j$ and \mathbf{A} is a block matrix with the size $M \times M$ matrix $\mathbf{A}_{i,j} = \mathbf{G}_i^H \mathbf{G}_j$ on block entry (i, j) ; it is defined as,

$$\mathbf{A} = \begin{bmatrix} \mathbf{A}_{1,1} & \mathbf{A}_{1,2} & \dots & \mathbf{A}_{1,NK} \\ \mathbf{A}_{2,1} & \mathbf{A}_{2,2} & \dots & \mathbf{A}_{2,NK} \\ \vdots & \vdots & \ddots & \vdots \\ \mathbf{A}_{NK,1} & \mathbf{A}_{NK,2} & \dots & \mathbf{A}_{NK,NK} \end{bmatrix}. \tag{3.10}$$

To maximize the trace of the Fisher information, we define another matrix $\mathbf{A}_{tr} \in \mathbb{R}^{NK \times NK}$ where each entry is $[\mathbf{A}_{tr}]_{i,j} = \text{trace}(\mathbf{A}_{i,j})$. The suboptimal optimization formulation can then be expressed as,

$$\begin{aligned} \max \quad & \text{trace}(\mathbf{F}(\mathbf{x})) = \mathbf{c}^H \mathbf{A}_{tr} \mathbf{c} \\ \text{s.t.} \quad & \|\mathbf{c}\|^2 = 1. \end{aligned} \quad (3.11)$$

It is clear that (3.11) can be handled by the Lagrangian function [39]. Set λ as the Lagrangian multiplier, the Lagrangian function can be written as,

$$L(\mathbf{c}, \lambda) = \mathbf{c}^H \mathbf{A}_{tr} \mathbf{c} - \lambda(\|\mathbf{c}\|^2 - 1). \quad (3.12)$$

The optimal solution is found by taking the partial derivatives of (3.12) with respect to \mathbf{c} and λ and setting them to be equal to zero, which gives,

$$\mathbf{A}_{tr} \mathbf{c} = \lambda \mathbf{c}. \quad (3.13)$$

This indicates that \mathbf{c} is an eigenvector of \mathbf{A}_{tr} with λ as its eigenvalue. Since the goal is to maximize the cost function, the solution should be finding the eigenvector of \mathbf{A}_{tr} corresponding to the largest eigenvalue.

It is important to note that the matrix \mathbf{A}_{tr} is of complex nature, leading to its leading eigenvector also being complex. However, this thesis restricts its focus to amplitude and bi-phase encoding with discrete angles of 0 and 180 degrees out of simplicity. Thus the encoding matrix \mathbf{C} is constrained to the real domain. Decompose the cost function in (3.11) into the real and complex parts, it can be written as

$$\text{trace}(\mathbf{F}(\mathbf{x})) = [\mathbf{Re}[\mathbf{c}]^T \quad \mathbf{Im}[\mathbf{c}]^H] \begin{bmatrix} \mathbf{Re}[\mathbf{A}_{tr}] \\ \mathbf{Im}[\mathbf{A}_{tr}] \end{bmatrix} \begin{bmatrix} \mathbf{Re}[\mathbf{c}] \\ \mathbf{Im}[\mathbf{c}] \end{bmatrix}. \quad (3.14)$$

Since only the real part of \mathbf{c} is taken into consideration for amplitude and bi-phase encoding, the imaginary part can be set to $\mathbf{Im}[\mathbf{c}] = \mathbf{0}$. (3.14) can thus be written as,

$$\text{trace}(\mathbf{F}(\mathbf{x})) = \mathbf{Re}[\mathbf{c}]^T \mathbf{Re}[\mathbf{A}_{tr}] \mathbf{Re}[\mathbf{c}]. \quad (3.15)$$

It is clear that the amplitude and bi-phase encoding matrix can be found by the leading eigenvector of the real part of the matrix \mathbf{A}_{tr} .

3.2 Encoding Matrix Optimization for Multiple Transmissions

In Doppler ultrasound imaging, to compensate for the resolution loss from the non-focus transmission, usually, L planewave transmissions with different angles are required to obtain one Doppler frame [2]. By transmitting planewaves at different angles, the ultrasound system can receive echoes from various directions. This allows for the construction of a higher resolution and contrast compounded image because each angle provides unique information about the structure being imaged, allowing for a more accurate representation.

In this thesis, we focus on designing L different encoding matrices for the L transmissions to aid in constructing a more accurate compound ultrasound image. Assuming the pixel intensity \mathbf{x} remains constant across these L transmissions, a signal model for L transmissions and measurement events can be written as follows,

$$\mathbf{y} = \begin{bmatrix} \mathbf{y}_1 \\ \mathbf{y}_2 \\ \vdots \\ \mathbf{y}_L \end{bmatrix} = \begin{bmatrix} \mathbf{G}(\mathbf{C}_1) \\ \mathbf{G}(\mathbf{C}_2) \\ \vdots \\ \mathbf{G}(\mathbf{C}_L) \end{bmatrix} \mathbf{x} = \mathbf{G}(\mathfrak{C})\mathbf{x}. \quad (3.16)$$

It can be seen that model (3.16) is still linear with respect to \mathbf{x} and the encoding matrices \mathbf{C}_l , thus the same optimization methods described in sections 3.1.1 and 3.1.2 can be applied to solve it.

Leading Eigenvectors Transmissions

Solving for encoding matrices in (3.16) using the optimization function (3.8) described in section 3.1.1 would still encounter memory issues when implemented due to the large number of pixels. However, the suboptimal solution (3.11) discussed in section 3.1.2, which involves maximizing the trace of the Fisher information matrix, would result in identical encoding matrices for all L transmissions, i.e., $\mathbf{C}_1 = \mathbf{C}_1 = \dots = \mathbf{C}_L$. This is because when maximizing the Fisher information matrix for (3.16), it will maximize for each $\mathbf{G}(\mathbf{C}_l)$ matrix separately and this will give an identical encoding matrix \mathbf{C} , which is not ideal for multiple transmissions as we desire different encoding matrices for each transmission.

To address this challenge, an alternative approach can be considered. In the suboptimal solution, the optimized encoding matrix for one transmission is found by the leading eigenvector of the real part of matrix \mathbf{A}_{tr} . By examining the eigenvalues of $\mathbf{Re}[\mathbf{A}_{tr}]$ (as shown in Figure 3.1), multiple large eigenvalues are observed in close proximity to each other, indicating the presence of multiple suboptimal solutions. Therefore, utilizing the first few leading eigenvectors corresponding to these large eigenvalues for multiple transmissions could be a potential solution. The feasibility and effectiveness of this approach will be further discussed in the next chapter.

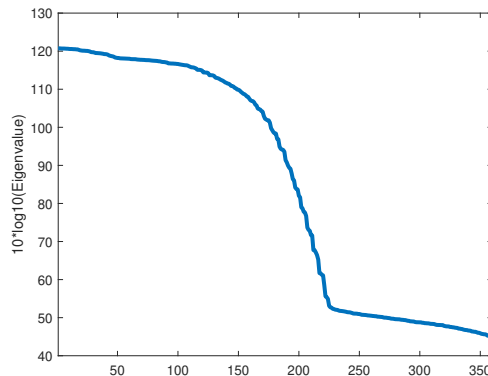


Figure 3.1: Eigenvalues of matrix $\mathbf{Re}[\mathbf{A}_{tr}]$.

3.3 Constraints in the Problem

To implement the optimized encoding matrix in a real-world experimental setup, for example, to image blood vessels in a mouse brain, there are some physical and hardware constraints that should be taken into consideration.

First, the maximal duration of the coded pulse is bounded and determined by the blind area allowed in the image. This is because the ultrasound device cannot receive backscattered echo until the transmission process is over. Therefore, the longer the transmitted pulse, the larger the near-field blind area is. The relationship between the duration of the pulse t_{pulse} and the depth of the blind area d_{blind} is,

$$t_{pulse} = \frac{2d_{blind}}{c_0}, \quad (3.17)$$

where c_0 is the propagation speed of the ultrasonic wave, which in this case is 1540 m/s. For a mouse brain imaging setup, the probe is fixed at least 4 mm above the mouse brain. The reason for this offset is that the elevational focus starts to build up only after this propagation distance, therefore there is at least a 4 mm dead zone. Using (3.17), we have $t_{pulse} \leq 5.19\mu s$.

Second, the number of transmissions L per compound image is bounded by the desired Doppler frequency f_D and maximum imaging depth d_{image} . Assume that we want to achieve a 500 Hz Doppler frequency, compliance with the Nyquist theorem $f_D < f_{samp}/2$, the sampling frequency f_{samp} should be set to at least 1 kHz. The maximum imaging depth is set to $d_{image} = 11$ mm, therefore, the maximal firing rate can be calculated as $c_0/2(d_{image} + d_{blind}) = 51$ kHz.

If the sampling frequency f_{samp} is set to be 1 kHz, the optimal approach would involve acquiring images at this frequency while employing coherent compounding. The number of transmissions per compound image is determined by the firing frequency of the probe. However, the previously calculated maximal firing rate of 51 kHz is often infeasible in practice. It is necessary to introduce a dead time between transmissions to accommodate reverberations on the remaining skull bone or other interfaces [2]. This dead time also serves to reduce the probe duty cycle, as continuous firing could result in heat-induced damage. Striking a balance, a practical compromise involves halving the theoretical maximum firing frequency, yielding an experimental firing rate of 25 kHz. Moreover, Montaldo et al. experimentally validate that when L reaches 9, the resulting contrast and SNR are already satisfying and when it is larger than 16, the gain in SNR and image contrast will only have little improvement [20]. Therefore, a L between 10 and 16 should be sufficient enough.

Simulation Results

To validate the effectiveness of the optimized encoding matrix, simulation experiments are conducted using the K-Wave. K-Wave is a specialized numerical simulation toolbox widely utilized for modeling and simulating the propagation of acoustic waves in complex media [40]. Due to computational memory constraints, the suboptimal optimization function (3.11) discussed in section 3.1.2 is used to generate optimized encoding matrices. In this approach, the optimized encoding matrix is obtained through the leading eigenvector of the matrix $\mathbf{Re}[\mathbf{A}_{tr}]$.

Two distinct scenarios were considered to evaluate the performance of the proposed optimized code. The first scenario involved a smaller array with an element pitch-to-wavelength ratio, denoted by $pitch/\lambda$, less than 0.5. The objective was to assess the capabilities of the optimized code in cases where the array elements are relatively closely spaced compared to the operating wavelength.

The second scenario aimed to test the optimized code on a larger array that violates the Nyquist sampling frequency condition, with a pitch-to-wavelength ratio approximately equal to 1. Both sampling conditions can be found in clinical hardware where large, sub-Nyquist element probes are often referred to as linear arrays, and small element probes are named phased arrays.

By conducting these simulation experiments, we sought to verify the efficiency and reliability of the proposed encoding matrix optimization method and to ascertain its suitability for both closely spaced and sub-Nyquist-sampled large arrays. The results of these experiments provide crucial insights into the method's practicality and its potential for real-world applications.

4.1 Small Array

The small array used in this thesis comprises 128 elements with a pitch of $25\mu m$ between adjacent elements. The imaging area consists of equidistantly placed point scatters. The experimental setup is illustrated in Figure 4.1. The ultrasound transducer emits a base pulse with a center frequency of 15 MHz. The region of interest for imaging spans from a depth of 4 mm to 11 mm, which is analogous to the imaging region for mouse brain studies.

An optimized encoding matrix of size 128×5 is designed, which means the pulse has a bit-length of 5. This chapter aims to compare the imaging performance of four different transmission methods: single short pulse planewave, 5-bit Barker code, 5-bit random code, and 5-bit optimized code. All the codes are normalized to have the same average energy before transmission. The transmit pulse shapes in the time domain for these four methods are depicted in Figure 4.2, along with the frequency spectrum of the single short pulse (base pulse).

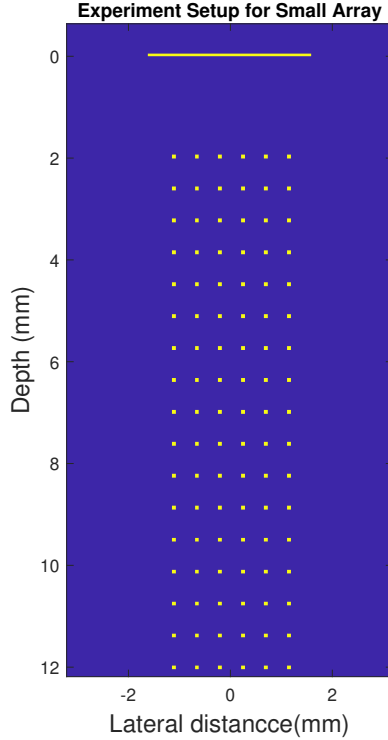
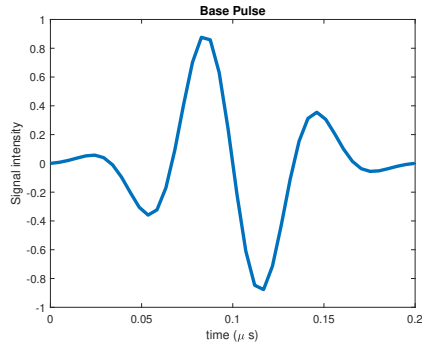


Figure 4.1: Experiment setup in K-Wave for a small array with 128 elements and $25\mu\text{m}$ pitch. The imaging area is a set of equidistantly placed point scatters.

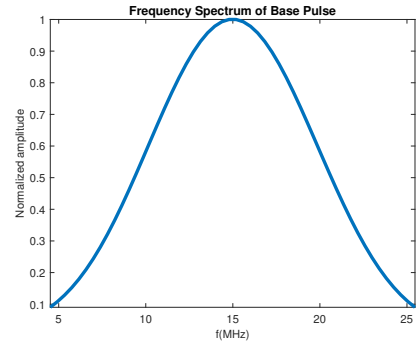
To compare the quality of a single ultrasound compounded image, images from L transmissions are compounded. For the optimized multiple transmission case, the leading eigenvectors transmission scheme as described in section 3.2 is employed. When maximizing the Fisher information matrix, an image subset between 6 to 11 mm in Figure 4.1 was chosen for optimization. The corresponding encoding matrices are shown in Figure 4.3. Initially, the wave propagation pressure field and the imaging results obtained using the L leading eigenvectors transmissions were investigated.

Figure 4.4 shows the pressure field from 10 leading eigenvectors transmissions and their corresponding imaging results. The pressure field is obtained by placing sensors at every grid point in the imaging area and measuring its maximum pressure. The images here are obtained using matched filtering. Figure 4.4 shows that each eigenvector transmission yields a different focusing area in the image, and their corresponding imaging results exhibit variations. For instance, the second eigenvector focuses more on the two sides of the image, while the third one has more energy transmitted to the middle. Even though the first and the fourth transmissions have similar pressure fields, their resulting image results are different. These findings highlight the need for different optimized encoding matrices for multiple transmissions.

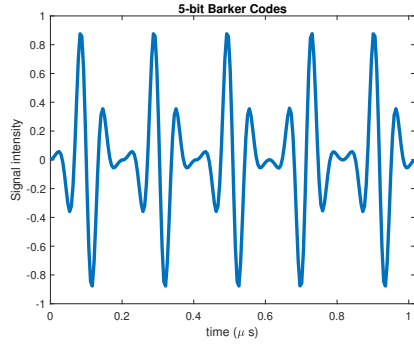
The number of transmissions L is determined by the Doppler frequency to be detected and the desired frame rate. However, another constraint can be considered on the number of leading eigenvectors transmissions to ensure a good compounded image



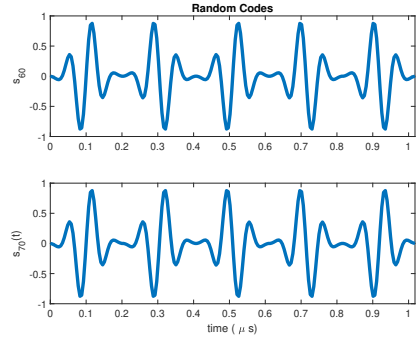
(a) Base pulse



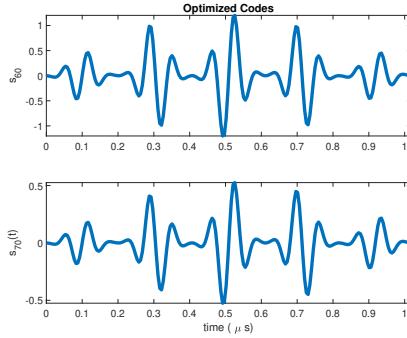
(b) Frequency spectrum of Base pulse



(c) 5-bit Barker codes



(d) 5-bit Random codes s_{60} and s_{70}



(e) 5-bit Optimized codes s_{60} and s_{70}

Figure 4.2: Transmit pulse shape for (a) single short pulse (base pulse), (b) frequency spectrum of base pulse, (c) 5-bit Barker codes, (d) 5-bit random codes on elements 70 th and 80 th, and (e) 5-bit optimized codes on elements 70 th and 80 th.

quality, which can be analyzed from the CRB perspective. The CRB is a lower limit that indicates the performance of an unbiased estimator: lower CRB values correspond to lower variance and better unbiased estimators.

Thus, how the CRB changes when compounding more leading eigenvectors for multiple transmissions is investigated. In Figure 4.6a, the normalized CRB (ranging from 0 to 1, where 0 represents perfect estimation and 1 indicates the worst estimation) is plotted for a pixel located at depths of 4.5 mm and 11 mm when compounding 1 to 40 leading eigenvectors transmissions. It becomes evident that after compounding

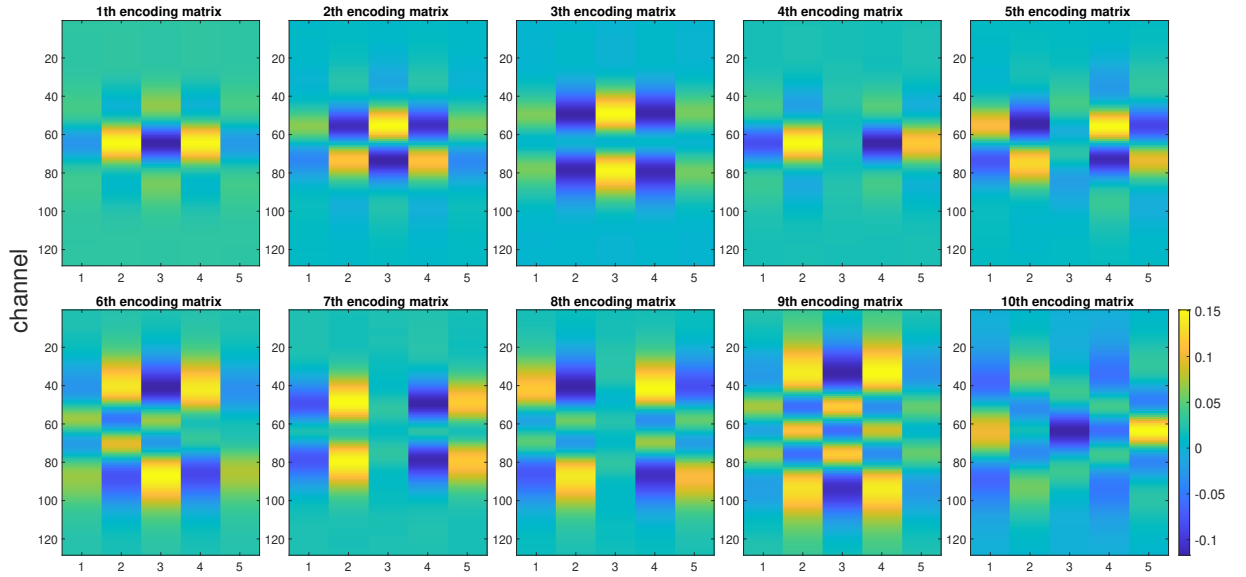


Figure 4.3: The ten optimized encoding matrices for the small array. The size of the matrices is 128×5 . The y-axis indicates the channels and the x-axis indicates the bit length. The color map shows the amplitude and bi-phase encoding value of the code.

5 transmissions, the CRB no longer decreases significantly, and for the pixel in the deeper area, it has already reduced to a low level. Taking the Doppler frequency into consideration, the number of transmissions L is set to 10 to ensure good compounded image quality.

Furthermore, a comprehensive investigation of the compounded imaging results obtained from the optimized code is conducted and compared with 5-bit Barker, single pulse planewave, and 5-bit random transmission methods. For each imaging scenario, the same level of white Gaussian complex noise was added to the measurement data at a signal-to-noise ratio of 10 dB. The corresponding results are illustrated in Figure 4.5.

The image on the left represents the outcome of the optimized code, obtained by compounding data from 10 leading eigenvectors transmissions. The second and third images display results from Barker-5 transmissions and single pulse planewave transmissions, respectively. Both of these involve compounding data acquired from 10 insonified angles spanning $[-12^\circ, 12^\circ]$. The fourth image is acquired and compounded through 10 instances of 5-bit random code transmissions.

The obtained results reveal that optimized transmission exhibits the highest SNR, particularly in the deeper area ranging from 7 to 9 mm. In contrast, both the Barker code and planewave transmissions show distortions starting at around 7 mm, where the scatters are not represented in a straight line. While Barker codes outperform planewave in the deeper region, they still fall short compared to optimized transmission. On the other hand, random transmission appears to be the most sensitive to additive noise, leading to a significant degradation in image quality.

It is important to note that there is a trade-off for the optimized code, as the achieved resolution is somewhat compromised compared to the other methods. This

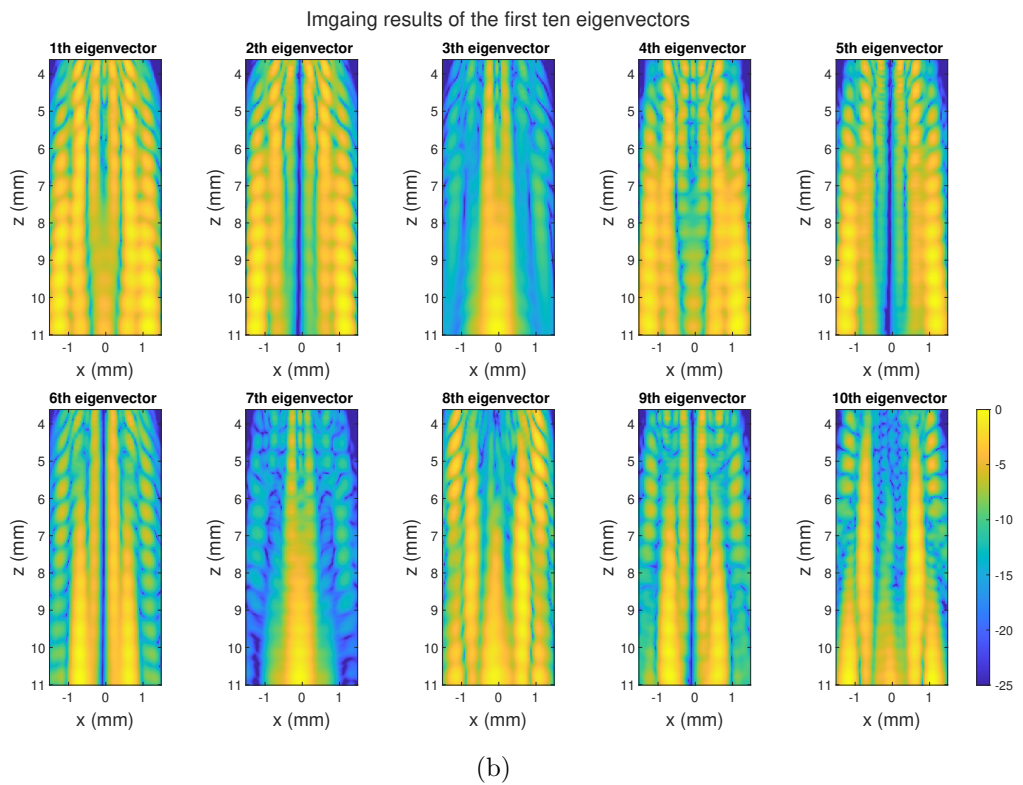
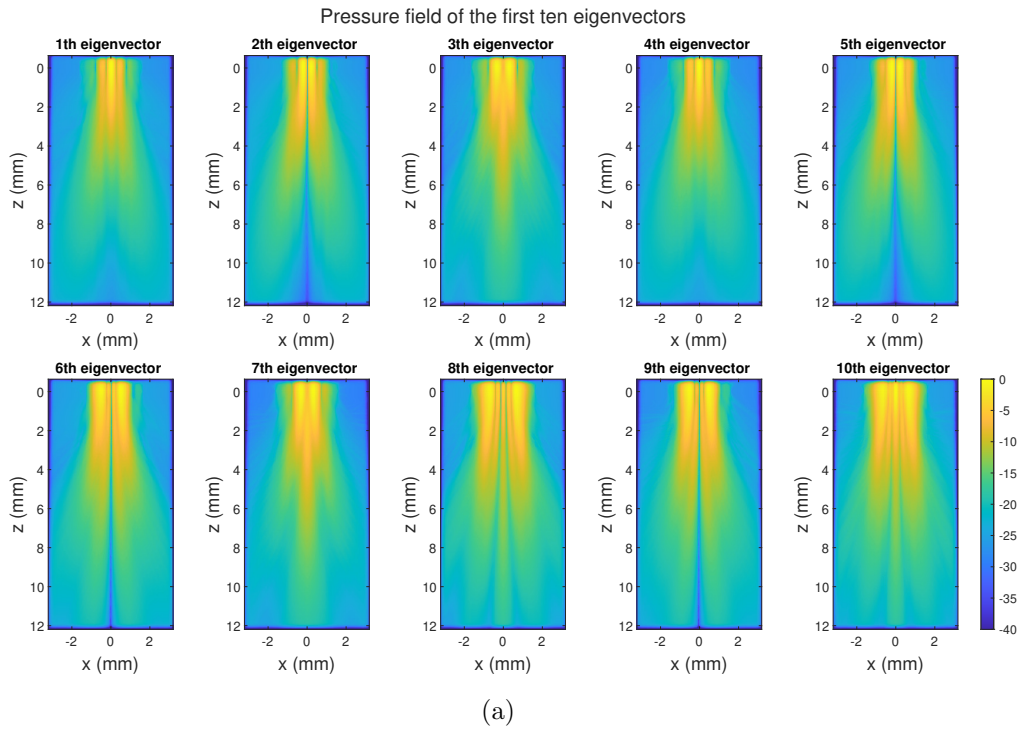


Figure 4.4: (a) shows the pressure field from 10 leading eigenvectors transmissions and (b) shows their corresponding imaging results.

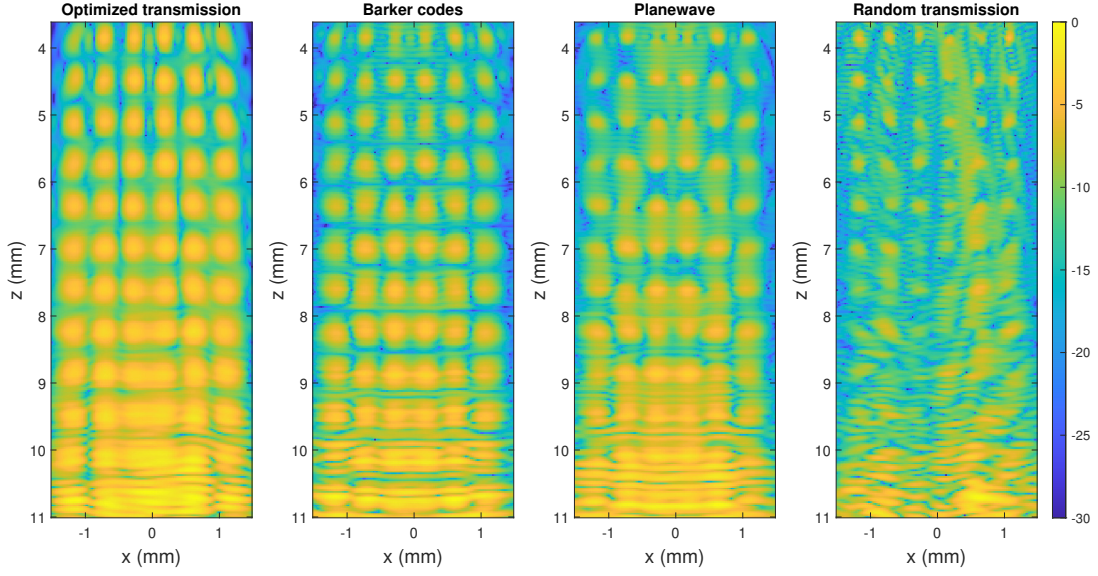


Figure 4.5: Imaging results comparisons between optimized transmissions, Barker codes transmissions, planewave transmissions, and random transmissions (On the figure from left to right). The same level of noise where $SNR = 10dB$ is added to each scenario.

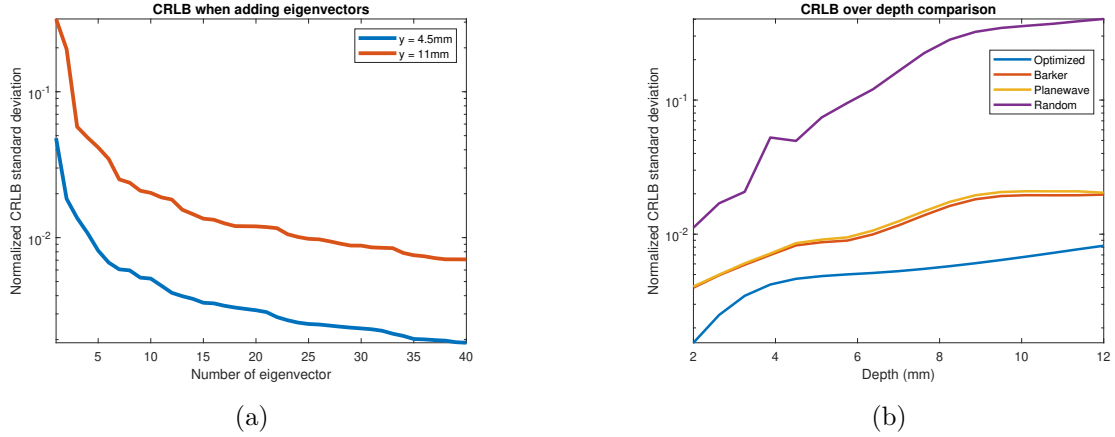


Figure 4.6: (a) shows the CRB over compounding eigenvectors for a pixel at depth 4.5 mm and depth 11 mm . (b) shows the CRB over depth for random, Barker, planewave, and optimized code. The results are after ten transmissions compounding.

phenomenon stems from the limitation in the optimization formulation (3.11), where the autocorrelation property of the code is not considered. The autocorrelation function (ACF) of the optimized code (on the 80th element) and the 5-bit barker codes are plotted in Figure 4.7 and the numerical analysis is shown in Table 4.1. It can be seen that the normalized mainlobe amplitude (the highest peak) of the optimized code (0.55) is higher than the Barker code (0.25) by a factor of 2. However, the mainlobe to sidelobe (the second highest peak) ratio of the optimized code is only 1.89 which is much lower than that of the Barker code (5). A high mainlobe level can result in a

higher SNR in the image but a low mainlobe to sidelobe ratio will cause a degraded resolution.

The CRB analysis is also performed to assess the estimation accuracy of the four different methods across the imaging depth, as depicted in Figure 4.6b. The results demonstrate that the optimized code yields the lowest CRB, indicating superior estimation precision. While the Barker code and short pulse planewave exhibit similar CRB curves, the former slightly outperforms the latter. On the other hand, the random code displays the highest CRB values, which is consistent with the imaging results. This analysis further confirms the effectiveness of the optimized code compared to the other tested methods in terms of both image quality and estimation accuracy.

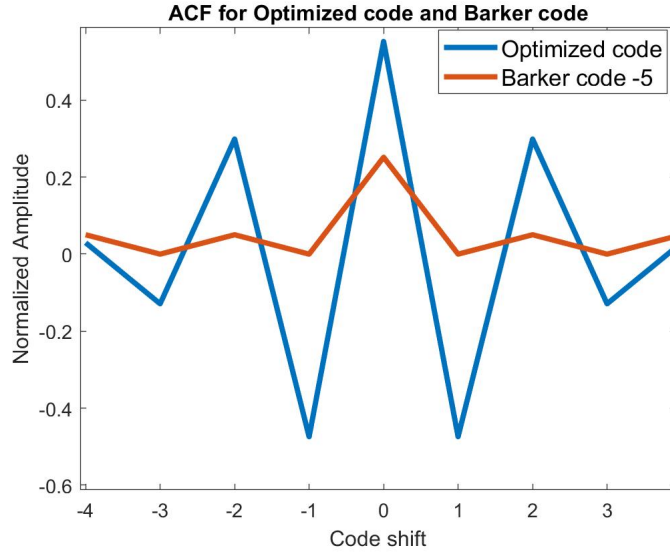


Figure 4.7: Autocorrelation function for optimized codes (on the 80th element) and Barker code of length 5.

Table 4.1: Autocorrelation function analysis for optimized codes (on the 80th element) and Barker code.

Code	Mainlobe amplitude	Sidelobe amplitude	Mainlobe to Sidelobe ratio
Optimized Code	0.55	0.29	1.89
Barker Code	0.25	0.05	5.00

4.2 Large Array

In this section, the applicability of the proposed optimized encoding matrix is investigated in a realistic scenario using the Verasonics L22-14v high-frequency probe setting, commonly employed in mouse brain blood flow imaging. This probe consists of 128 elements with a 0.1 mm element pitch. The center frequency for transmitting pressure pulses remains at 15 MHz and the wavelength λ is 0.102 mm. Same as the previous

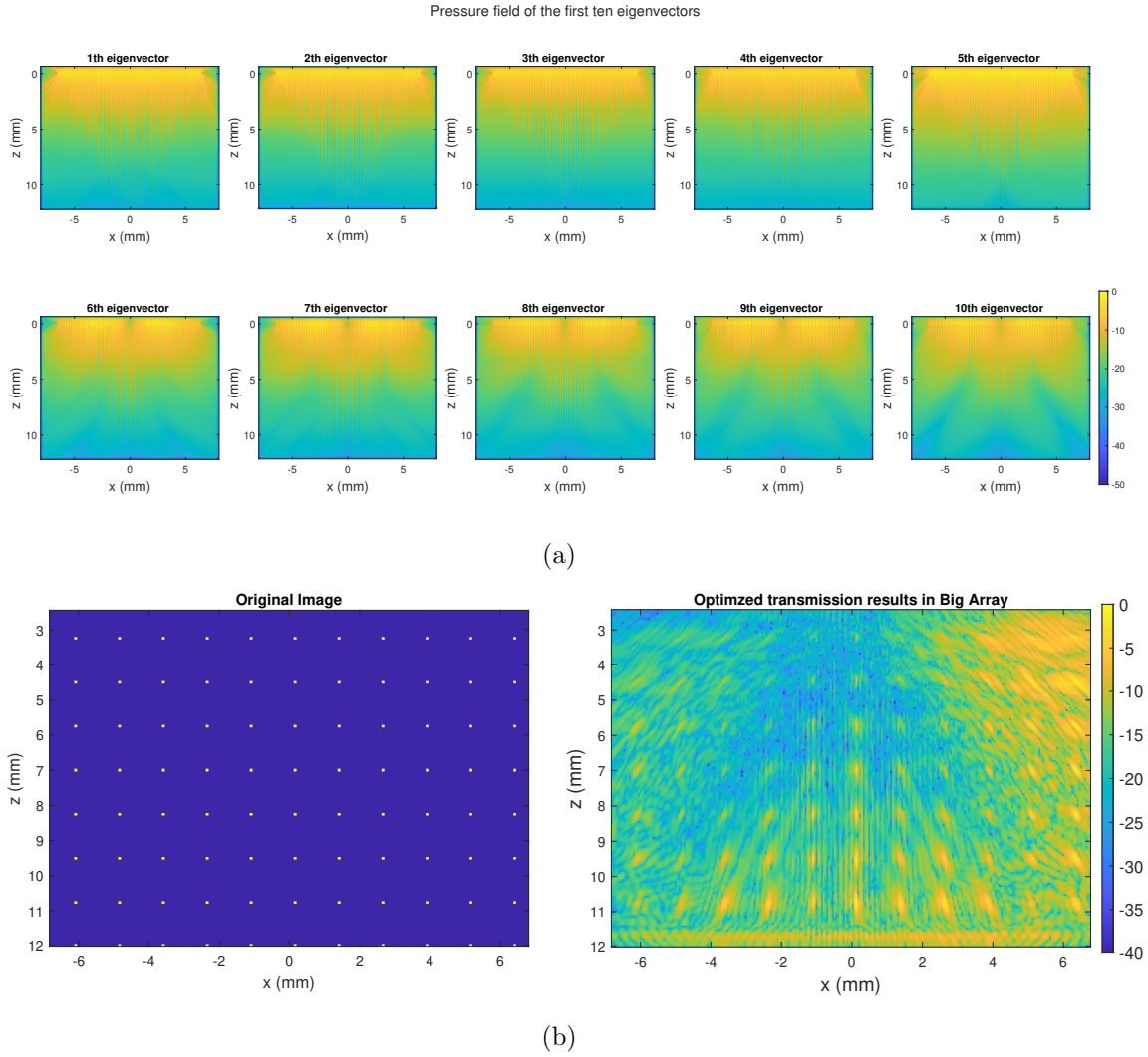


Figure 4.8: (a) shows the pressure field from 10 leading eigenvectors transmissions and (b) shows their corresponding imaging results for the large array with a transmitting center frequency of 15 MHz.

section, an encoding matrix of size 128×5 is optimized for an image subset from 6 to 11 mm.

Figure 4.8 presents the transmitting pressure field for the first ten leading eigenvectors, along with the compounding imaging result. The pressure fields show that the transmitting waves do not have the focusing ability in the focused area (6 to 11 mm) and there are clear grating lobes existing in the transmitting beams. The compounded image as shown in Figure 4.8b shows clear distortion and blurring for scatters. The scatters are either elongated (the middle area between 9 to 12 mm) or slanted (scatter points at two sides). Scatters in near-field areas are blurring, making it difficult to distinguish the shapes. The results are not satisfactory, and there are two primary reasons behind this outcome.

Firstly, the pitch-to-wavelength ratio ($0.1 / 0.102$ mm) is close to 1, the array does not meet the Nyquist sampling theorem requirement. Consequently, the array is operating under the Nyquist frequency, which might generate aliasing and negatively impact image quality. Aliasing occurs when the sampling rate is insufficient to accurately capture the high-frequency components of a signal, leading to the misrepresentation of these frequencies in the reconstructed image. As a result, fine details, such as small structures and tissue textures, might be poorly represented or entirely missing from the image.

Secondly, the large element size poses limitations on the beam steering mobility of the array [41]. This constraint becomes evident when considering the beam spread equation (4.1), where θ_{max} represents the maximum steering angle of a single element, λ denotes the wavelength, and e corresponds to the element width. The larger the pitch-to-wavelength ratio, the smaller the steering angle.

$$\sin \theta_{max} = 0.514 \frac{\lambda}{e} \quad (4.1)$$

To further assess the focusing ability, experiments were conducted using the L22-14v probe configuration as can be seen in Figure 4.9. The probe transmitted a 5 MHz pulse and focused at three distinct points within the imaging area: left, middle, and right sections. The objective was to compare the focusing capability of this configuration with a 15 MHz excitation signal. The results clearly indicate that when the wavelength increases while maintaining the same element width, both the beam steering and focusing ability improve.

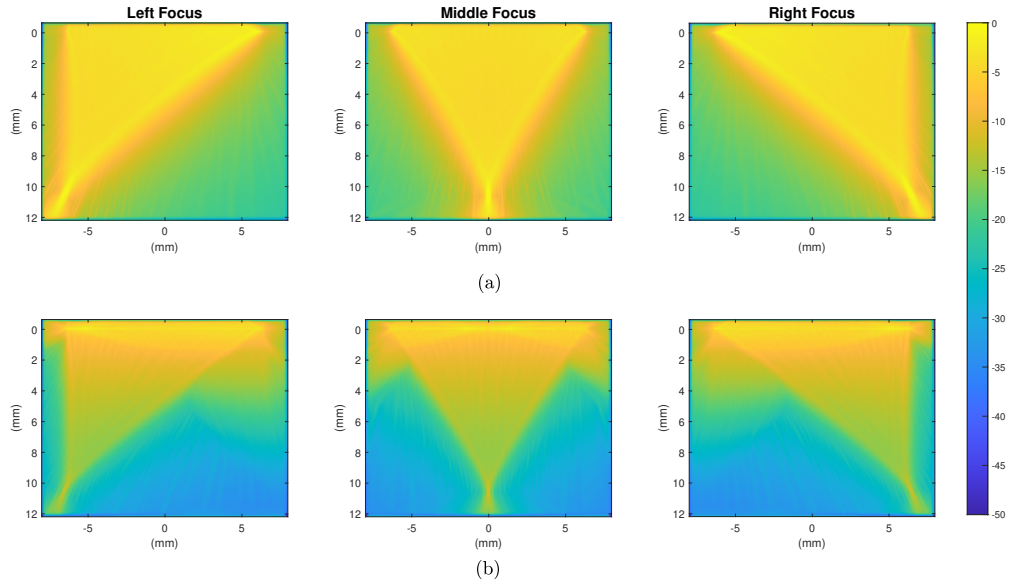


Figure 4.9: Beam steering and focusing ability demonstration for different frequency excitation pulse. (a) shows the pressure field for a 5 MHz excitation pulse when focusing at a point on the left, middle, and right side of the imaging area respectively from left to right. (b) shows the results for a 15 MHz excitation pulse.

The proposed encoding matrix optimization method aims to enhance the information retrieval from the focusing area and achieve a transmit beam that optimally covers the entire imaging area. However, the physical limitations imposed by the large array size and corresponding element pitch present challenges in achieving a focused beam that covers the focused area effectively. Consequently, for arrays operating below the Nyquist sampling frequency, a planewave transmit beam pattern is more suitable.

By employing a planewave transmit beam pattern, the limitations imposed by the physical constraints of the array can be mitigated. This beam pattern allows for uniform coverage of the imaging area, compensating for the challenges posed by the large element pitch. Therefore, in the case of arrays operating at sub-Nyquist frequencies, the planewave configuration becomes a preferable choice to ensure better image quality and adequate beam steering capabilities.

4.3 Clinical Transducer Results

As the optimized encoding matrix exhibits limited efficacy for large linear arrays that operate at the sub-Nyquist sampling frequency, our focus shifts toward assessing the performance of the optimized code through the utilization of an alternative clinical transducer. This section seeks to broaden the scope of evaluation and glean insights into the adaptability and effectiveness of the optimized encoding matrix across diverse transducer configurations. The M5Sc-D phased array transducer manufactured by General Electric (GE) presents an appealing option, with its 80×3 elements and a pitch of 0.27 mm. Operating at a center frequency of 2.8 MHz with wavelength $\lambda = 0.55$ mm, this transducer complies with the Nyquist sampling requirement. It is worth noting that for this thesis, we only consider using the middle row elements, resulting in a total of 80 active elements.

4.3.1 B-mode results

Simulations are conducted using point scatters placed equidistantly within the imaging area. The encoding matrix \mathbf{C} was optimized with dimensions 80×5 and an image subset between 50 mm to 90 mm area was chosen for optimization. Ten optimized encoding matrices are shown in Figure 4.10. Its performance was compared to 5-bit Barker code, single pulse planewave, and 5-bit random code. The imaging region spans from 5 mm to 90 mm. Figure 4.11 displays the results obtained from 10 transmissions compounding with the same level of additive white Gaussian noise (SNR = 10 dB).

Observing the results, it becomes evident that in the deeper area (starting from 55 mm), the optimized code outperforms the Barker code and planewave in terms of detectability. The 5-bit Barker code exhibits a slight deterioration in axial resolution compared to planewave, leading to visible sidelobes at point targets. This is due to the fact that the Barker code does not possess perfect sidelobe cancellation after pulse compression, resulting in sidelobe energy at approximately $1/5$ of the mainlobe energy [16]. On the other hand, the random code exhibits good axial resolution compared to the other methods, particularly in the near-field area, as reported in [27]. However, the contrast-to-noise ratio of the random code is significantly lower than other methods.

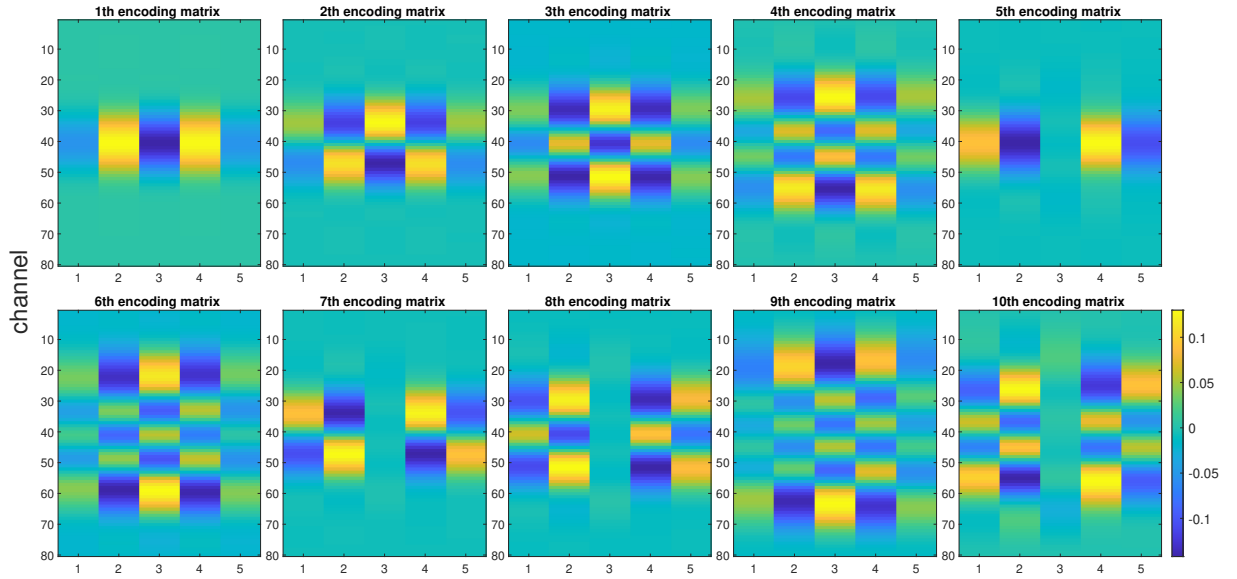


Figure 4.10: The ten encoding matrices of the M5Sc-D phased array transducer. The encoding matrices have a size of 80×3 . The y-axis indicates the channels and the x-axis indicates the bit length. The color map shows the amplitude and bi-phase encoding value of the code.

One of the trade-offs of using the optimized code is that the axial resolution is degraded, as also observed in Figure 4.5. This is attributed to the fact that the proposed optimization method did not consider the autocorrelation property of the codes, which is detailed in section 4.1. The optimization problem (3.11) focuses on optimizing the information within the Region of Interest (ROI) but does not guarantee the image resolution. In contrast, Barker codes are specifically designed to have good autocorrelation properties, allowing for retrieval of axial resolution comparable to that of single short pulses after matched filtering, as discussed in section 1.4.

Another tradeoff of using the optimized code is that it results in a narrower field of view compared to other methods. As evident from the first plot in Figure 4.11, the top left and right point scatters are not detectable. The reason behind this is that when optimizing for the encoding matrix using the suboptimal formulation (3.11), a focusing area was chosen between 50 to 90 mm in the imaging area. Since the near field is not taken into account when optimizing for the encoding matrix, there might exist some information loss in the near field area.

The results are quantitatively analyzed by computing the SNR of each point scatter in the four scenarios and comparing the performance. The calculation is as followed,

$$SNR = \frac{\overline{PW}_p}{\overline{PW}_b}, \quad (4.2)$$

where \overline{PW}_p and \overline{PW}_b are the mean energy value of the point scatter and the background noise, respectively. The box plots of the SNR data from each method are shown in Figure 4.12. In each box, the bottom and top edges of the box represent the 25th and 75th percentiles in the data, and the red line inside the box marks the median. The

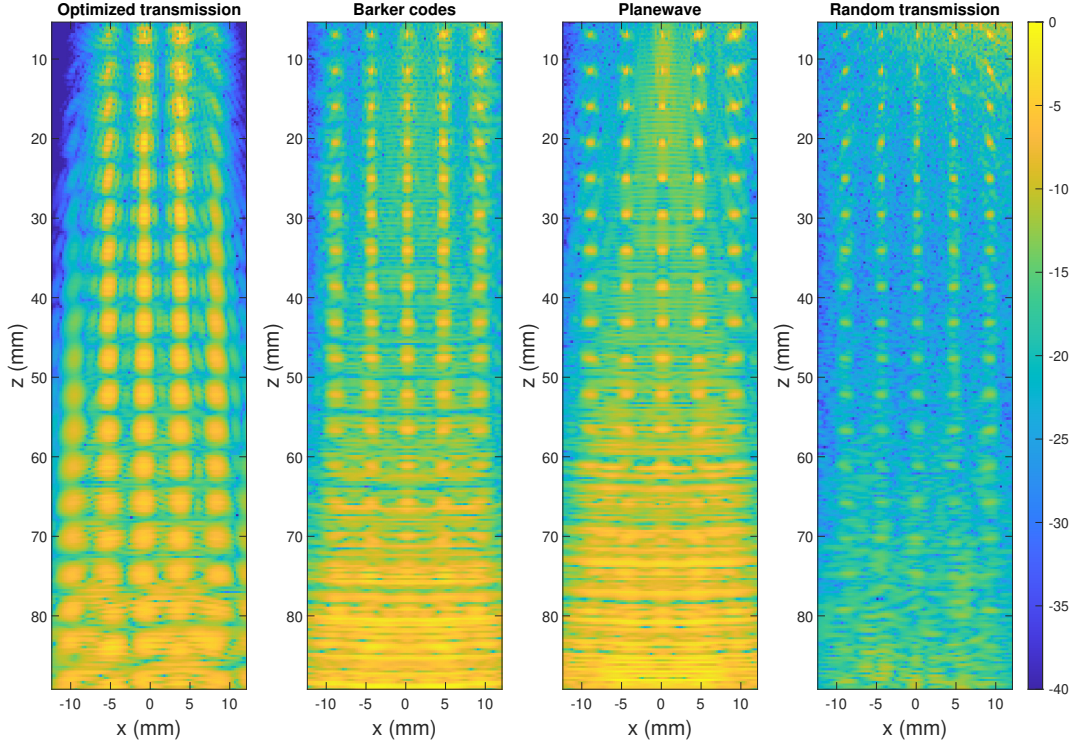


Figure 4.11: Imaging results comparisons between optimized transmissions, Barker codes transmissions, planewave transmissions, and random transmissions (On the figure from left to right) in GE probe setting. The same level of noise where $SNR = 10dB$ is added to each scenario.

whiskers represent the highest and lowest values in the data. The numerical results are corresponding with the imaging results. The optimized code has an overall higher SNR compared to other methods. Single pulse planewave has the highest variation. If we look at the median SNR value, the optimized code has a $GSNR = 4.4$ dB while the Barker code has a $GSNR = 2.5$ dB compared to the single short pulse. Compared to single pulse and random code, the optimized code and Barker code maintain a more consistent SNR performance.

In this thesis, the performance of different bit-length optimized codes (3-bit, 5-bit, and 10-bit) is investigated and compared. The results are illustrated in Figure 4.13 and 4.15.

As the bit-length increases, the SNR also increases. This is expected because longer codes have higher mainlobe levels after pulse compression, resulting in a stronger signal relative to the noise. In the deeper areas of the image, the longer codes exhibit higher resilience to noise. The increased bit length enables better detection of weaker signals from deeper structures, as these signals are less likely to be obscured by noise.

However, the use of longer codes also involves a trade-off. The 10-bit code, being the longest among the tested options, demonstrate certain disadvantages. Specifically, it exhibits lower resolution for point scatters compared to the 3-bit and 5-bit codes. This observed disadvantage of the 10-bit codes has been previously discussed in the thesis

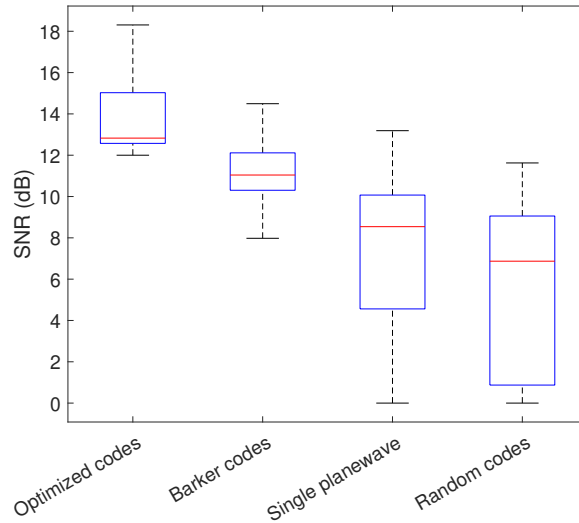


Figure 4.12: The SNR boxplot analysis for point scatterers images with (From left to right) optimized codes, barker codes, single pulse planewave, and random codes. In each box, the bottom and top edges of the box represent the 25th and 75th percentiles in the data, and the red line inside the box marks the median. The whiskers represent the highest and lowest values in the data.

and is attributed to the characteristics of the optimization algorithm itself, which is that the autocorrelation property of the code is not considered. As can be seen from the autocorrelation function of 3-bit, 5-bit, and 10-bit optimized codes in Figure 4.14 and table 4.2, 10-bit code has the highest mainlobe amplitude but the lowest mainlobe to sidelobe ratio which is only 1.19. 3-bit code has the lowest mainlobe level but has a mainlobe to sidelobe ratio of 5, which is equal to the 5-bit Barker code.

Table 4.2: Autocorrelation function analysis for 3-bit, 5-bit, and 10-bit optimized code.

Code	Mainlobe amplitude	Sidelobe amplitude	Mainlobe to Sidelobe ratio
3-bit code	0.37	0.31	1.19
5-bit code	0.23	0.13	1.77
10-bit code	0.05	0.01	5.00

4.3.1.1 LSQR Imaging

In order to improve the resolution of the optimized code results, an iterative imaging technique named LSQR is employed instead of matched filtering [42]. This method iteratively updates and refines the solution of the signal model (2.9) based on a residual vector $\mathbf{r} = \mathbf{y} - \mathbf{G}(\mathbf{C})\mathbf{x}$. In each iteration, it computes the QR factorization of $\mathbf{G}(\mathbf{C})^H$ and solves for a triangular system to update the image vector \mathbf{x} . The algorithm converges when the residual errors reach the predefined threshold or the maximum number of iterations is reached. This approach is particularly useful for large and ill-conditioned

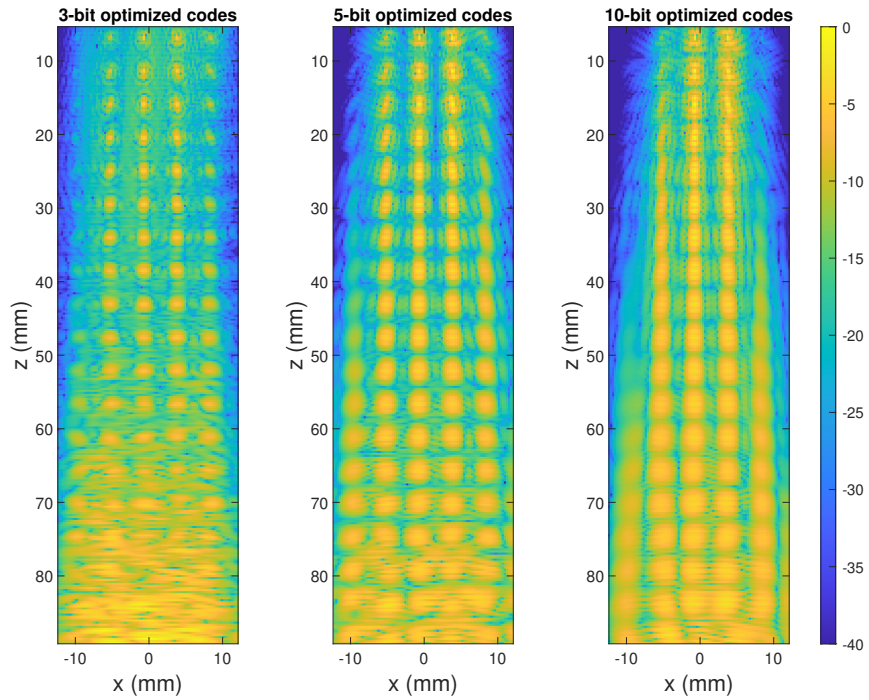


Figure 4.13: Imaging results from 3-bit, 5-bit, and 10-bit (from left to right) optimized codes. As the bit-length increases, the SNR of the image, especially in the deeper area is increased. The trade-off is a worsened resolution.

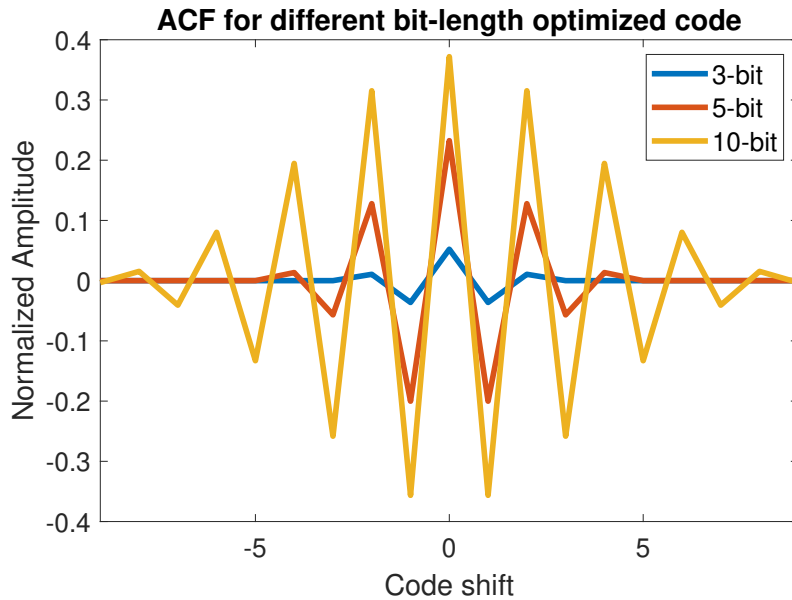


Figure 4.14: Autocorrelation function for 3-bit, 5-bit, and 10-bit optimized codes.

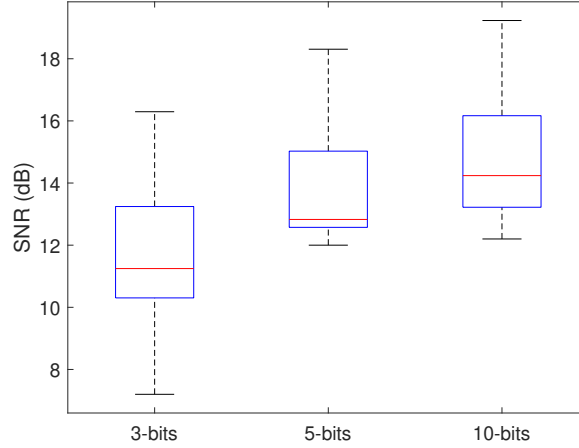


Figure 4.15: The SNR boxplot analysis for point scatter images with (From left to right) 3-bit, 5-bit, and 10-bit optimized codes. In each box, the bottom and top edges of the box represent the 25th and 75th percentiles in the data, and the red line inside the box marks the median. The whiskers represent the highest and lowest values in the data.

systems, which is the case in our study. A pseudo-code for the LSQR algorithm is presented in Algorithm 1.

Algorithm 1 LSQR Algorithm for Ultrasound Imaging

Data: Matrix $\mathbf{G}(\mathbf{C})$, Vector \mathbf{y} , Initial Guess \mathbf{x}_0 , Maximum Iterations i_{max} , Convergence Threshold ϵ

Result: Reconstructed Image Vector \mathbf{x}

```

1  $\mathbf{x} \leftarrow \mathbf{x}_0$ 
   $\mathbf{r} \leftarrow \mathbf{y} - \mathbf{G}(\mathbf{C})\mathbf{x}$ 
   $\mathbf{G}(\mathbf{C})^H \leftarrow$  Hermitian of  $\mathbf{G}(\mathbf{C})$ 
   $k \leftarrow 0$ 
2 while  $k < i_{max}$  and  $\|\mathbf{r}\| > \epsilon$  do
3    $\mathbf{Q}, \mathbf{R} \leftarrow$  QR Factorization of  $\mathbf{G}(\mathbf{C})^H \mathbf{r}$ 
    $\mathbf{b} \leftarrow$  Solve  $\mathbf{R}\mathbf{b} = \mathbf{Q}^H \mathbf{r}$  for  $\mathbf{b}$ 
    $\mathbf{x} \leftarrow \mathbf{x} + \mathbf{G}(\mathbf{C}) \cdot \mathbf{b}$ 
    $\mathbf{r} \leftarrow \mathbf{y} - \mathbf{G}(\mathbf{C}) \cdot \mathbf{x}$ 
    $k \leftarrow k + 1$ 
4 end

```

In order to assess the impact of increasing the number of iterations in LSQR imaging, experiments where we varied the number of iterations from 1 to 40 are conducted. Figure 4.16 displays images obtained at different iteration steps with a gap of 3. The results clearly show that as the number of iterations increases, the image resolution improves. However, after around 10 iterations, the image starts to overfit with the noise, leading to a decrease in the SNR in the deeper area. Interestingly, with the addition of more iterations, the point scatters at two sides at the top of the image

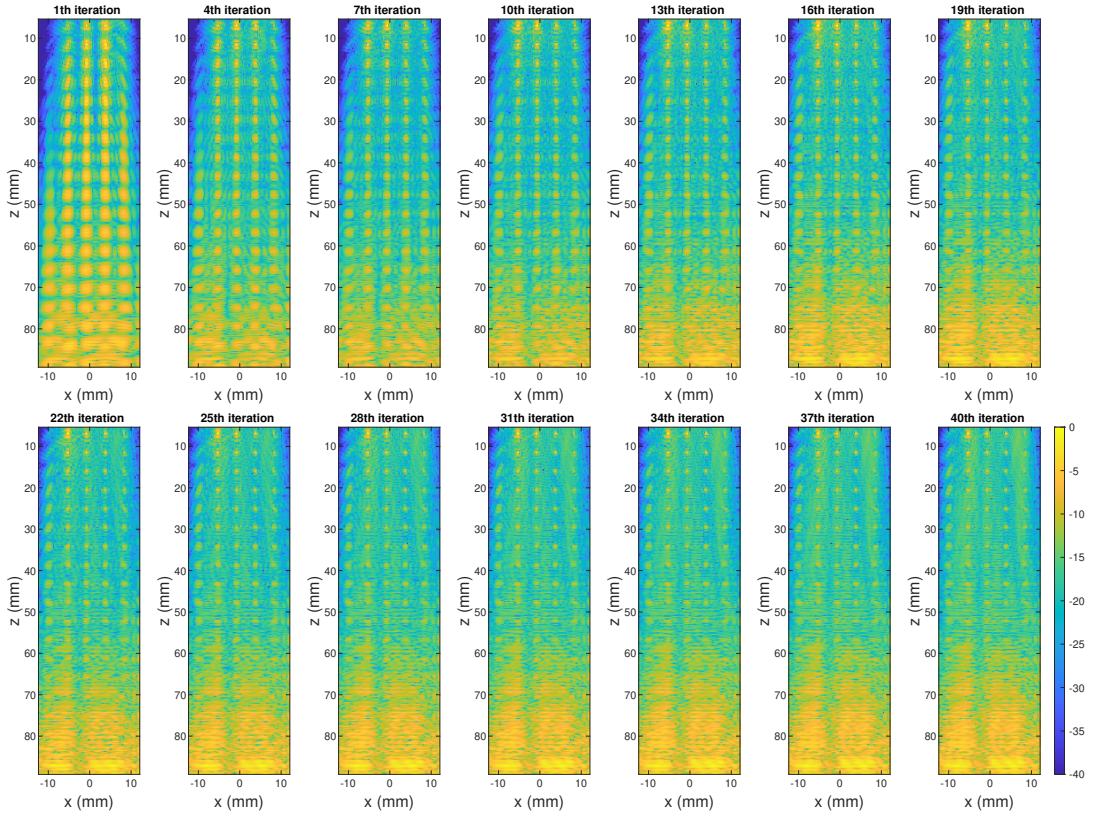


Figure 4.16: Optimized code imaging results using LSQR algorithm. Here we show the images after 1 to 40 iterations.

become detectable.

We also compared the LSQR results from the optimized code with those from the Barker code, as shown in Figure 4.18. The results indicate that LSQR does not significantly improve the image quality for the Barker code. Although the resolution improves slightly with an increase in the number of iterations, the near-field area starts to overfit with the noise after 4 iterations. Analyzing the normalized residual curve for these two coded excitation schemes reveals that the residual does not decrease significantly for Barker codes compared to optimized codes with the addition of more iterations (Figure 4.17).

In a direct comparison of the best performance image using LSQR between these two transmission schemes (e.g., the 10th iteration for optimized codes and the 4th iteration for Barker codes), the optimized codes still outperform Barker codes in terms of SNR in deeper areas while achieving nearly the same resolution. This can be visualized by looking at the image contrast, where a line from the image where the scatters are positioned is taken and plotted. If there is scatter in the position, a peak can be seen from the signal. Figure 4.19 shows the contrast signal for a vertical line located at position 0.24 mm in the image. Two methods both show clear peaks before 60 mm , with a comparable mainlobe-to-sidelobe ratio. The Barker code starts to fail in the deeper than 60 mm area where the peak got blocked by the noise, while the optimized

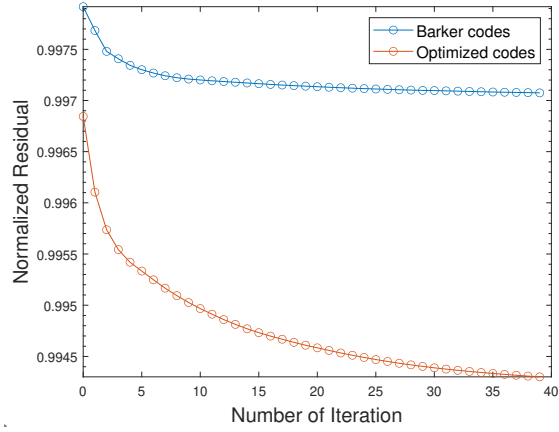


Figure 4.17: Normalized residual curves for Barker code and optimized code when adding iteration in LSQR.

code still maintains a good contrast.

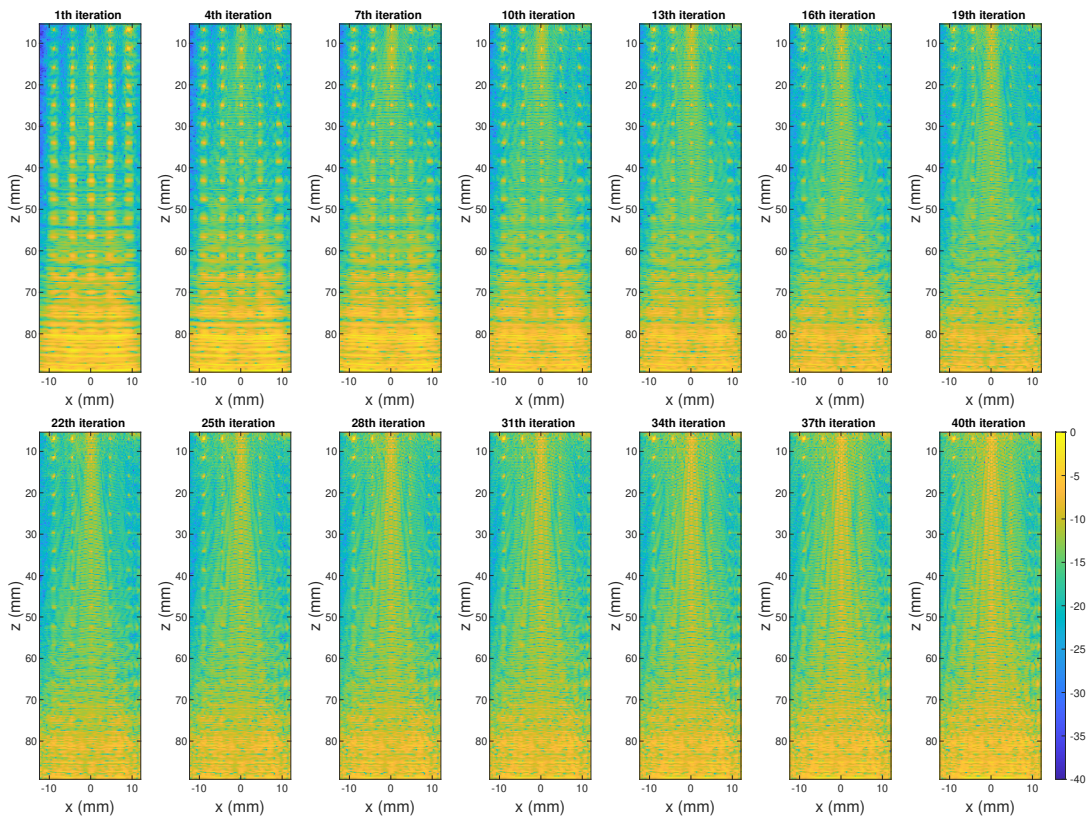


Figure 4.18: Barker code imaging results using LSQR algorithm. Here we show the images after 1 to 40 iterations.

In summary, LSQR imaging with optimized code shows notable improvements in

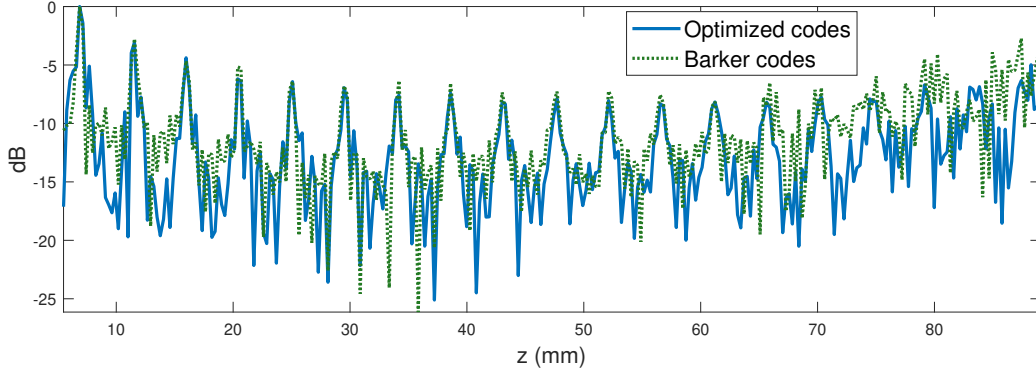


Figure 4.19: Image contrast to noise comparison between optimized code after 10 iterations and Barker code after 4 iterations. A vertical line from the image located at 0.24 mm is taken and plotted.

image quality as the number of iterations increases, leading to enhanced resolution and improved visibility of point scatters. However, the performance improvement plateaus after around 10 iterations due to noise overfitting. In contrast, LSQR does not provide significant improvements for Barker code, where the resolution slightly improves but the near-field area becomes more susceptible to noise overfitting. As a result, optimized code with LSQR imaging technique demonstrates superior image quality and SNR compared to Barker code under similar conditions.

4.3.2 Doppler Flow Simulations

In this section, blood flow imaging simulation is done in K-Wave using MATLAB. The clinical transducer setting described in section 4.3 is used here. A flow phantom with a size of $90 \times 20 \text{ mm}$ is generated with a 9 mm diameter parabolic blood vessel that is placed 55 mm away and angled at 25° from the transducer surface. The flow velocity is set to 9 cm/s and the blood-to-tissue level is -67 dB.

The imaging performance of 5-bit optimized code and 5-bit Barker code is compared. Still used 10 transmissions to get one compounded ultrasound image. For optimized code, the 10 leading eigenvectors are transmitted, and for Barker code, it is transmitted with 10 different angles ranging from -12° to 12° . The ensemble size is $N_e = 30$. The matched filter is used for beamforming and after compounding, an SVD filter is applied to all the temporal compounded images to gain the final power Doppler image.

Different levels of white Gaussian noise at the noise-to-blood level of -30, -15, and 0 dB are added to the measurement data. The results are shown in Figure 4.20, 4.21, and 4.22. The SNR and the Contrast-to-Noise ratio (CNR) are calculated for each image, where SNR is calculated using (4.2) and CNR is calculated as follows,

$$CNR = \frac{\overline{PW}_{vessel} - \overline{PW}_{tissue}}{std(PW_{tissue})}, \quad (4.3)$$

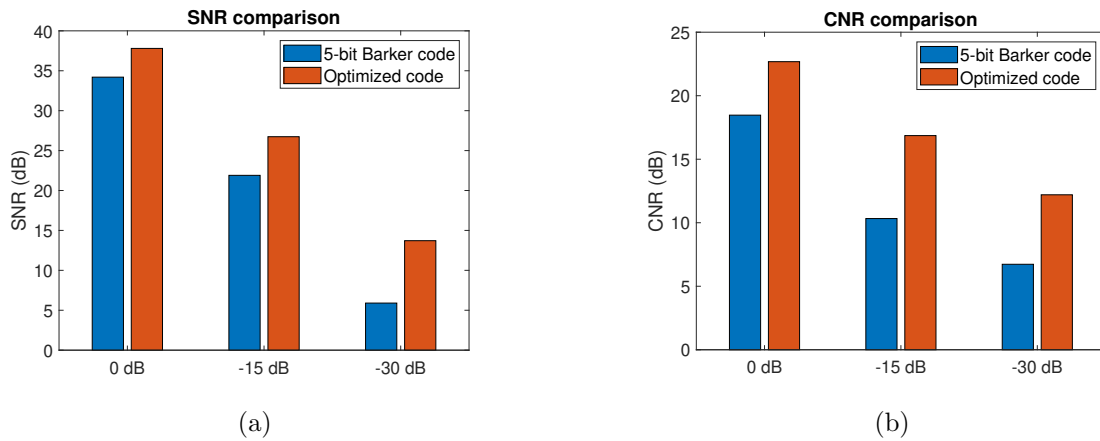


Figure 4.20: Numerical analysis of the performance of Barker code and optimized code. (a) shows the bar graph of the signal-to-noise ratio between Barker code and optimized code and (b) shows the bar graph of the contrast-to-noise ratio between Barker code and optimized code. They are calculated using the ROI shown in Figure 4.22, where the black rectangular indicated the blood vessel region and the white rectangular indicated the background region.

where the blood vessel area and the tissue area are indicated by the black and white rectangular in Figure 4.22 respectively.

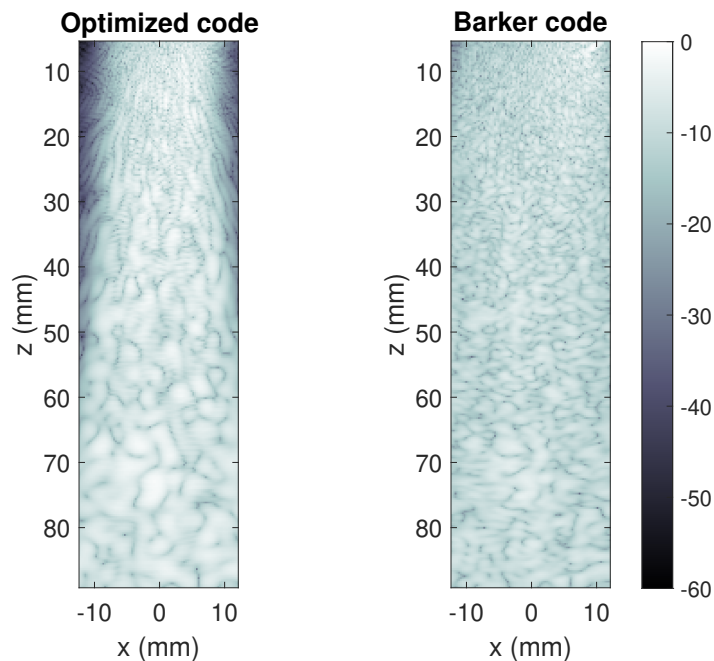


Figure 4.21: B-Mode images of the blood vessel from the optimized code and the Barker code.

The B-mode images are shown in Figure 4.21, where the blood vessels are completely masked by the tissue and noise. After SVD filtering, the PDI results of 0 and -15 dB noise level show that the blood vessel images from the optimized code have smoother

edges and stronger intensity compared to the ones from the Barker code (Figure 4.22). In the deeper area (below 80 mm), the optimized code exhibits darker background compared to the Barker code. For a high noise level (-30 dB), optimized code exhibits a clear advantage over the Barker code. The numerical results show that optimized code has consistent and higher SNR and CNR across different noise levels. For noise levels 0, -15, and -30 dB, the optimized code has SNR gains of 3.6, 4.84, and 7.81 dB compared to the Barker code. The optimized code is more robust to high level noise.

The blood flow simulation result demonstrates the ability of the proposed optimized code in improving the SNR of the Doppler images in deep areas. The resolution problems exhibited by the optimized code in the previous sections are not evident in the Doppler flow simulation.

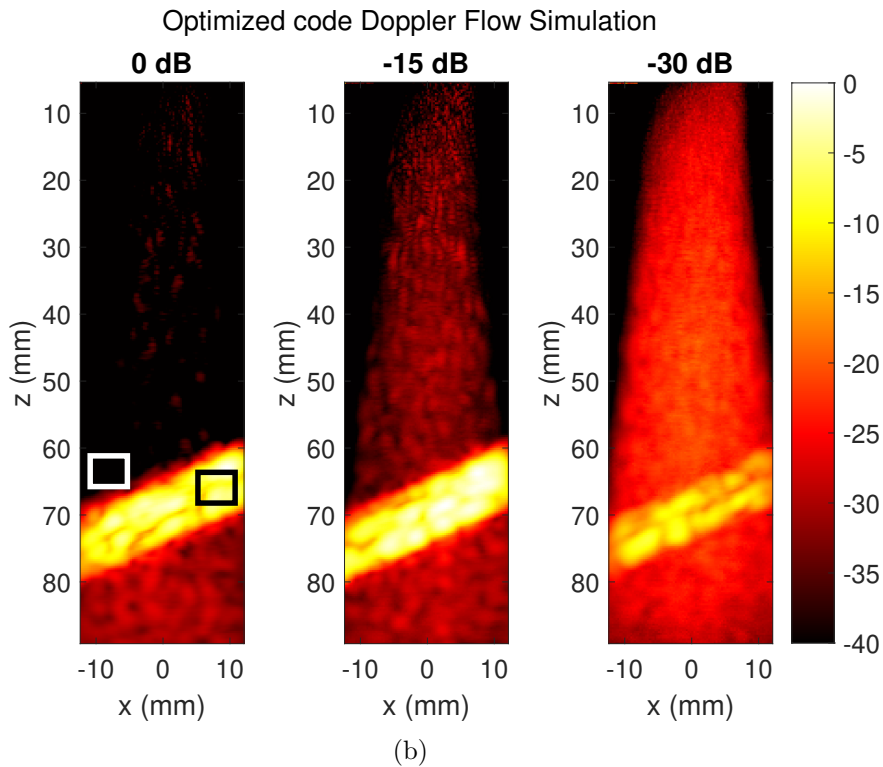
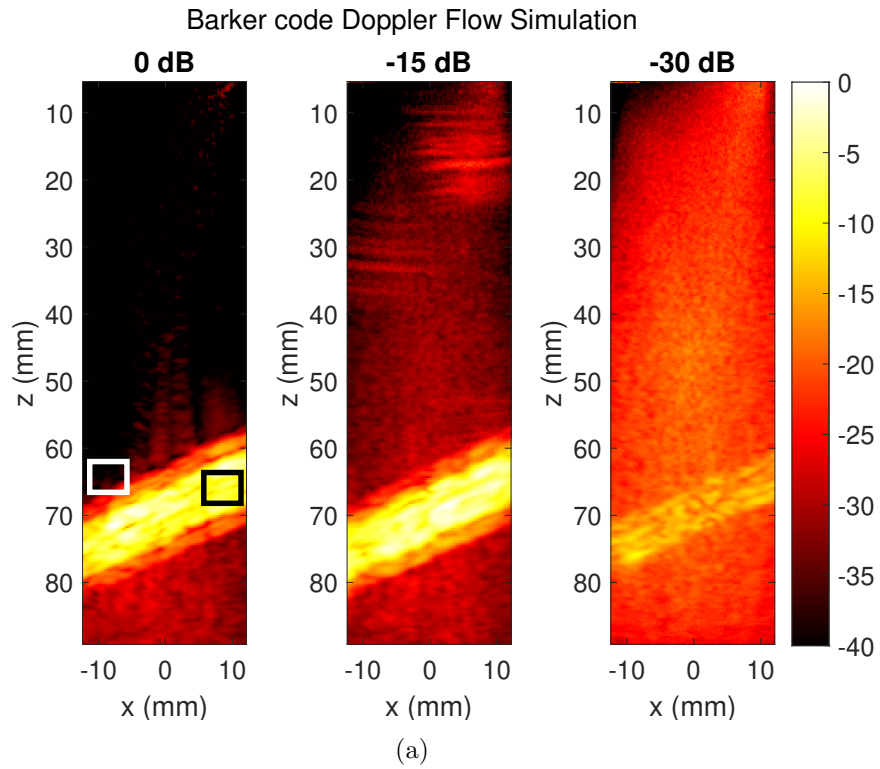


Figure 4.22: (a) shows the Power Doppler images from 5-bit Barker code with noise-to-blood levels at 0, -15, and -30 dB (from left to right). (b) is the Power Doppler images from the optimized code. All the images are shown with the same colormap spectrum from 0 to -40 dB.

In Doppler ultrasound imaging of cerebral blood flow, the visualization of small blood vessels in deep brain regions is often challenging due to the low SNR and a large dynamic range in the received signals. Coded excitation techniques have shown promise in enhancing SNR, particularly in deeper brain regions, as demonstrated in Figure 1.6. This thesis focuses on optimized code design for Doppler ultrasound imaging to improve on conventional coded excitation schemes, such as Barker codes, while using the same number of transmissions and bit-length. To design the optimized code is generalized and quantified into designing an encoding matrix \mathbf{C} , which is then incorporated into a linear measurement model described by equation (2.9). This linear signal model can be solved using efficient imaging techniques, such as matched filtering and least squares, especially when dealing with large systems. Amplitude encoding and bi-phase encoding are considered in this thesis, which constrain the encoding matrix \mathbf{C} to be real.

To find the optimized encoding matrix for a specific imaging area, a trace constraint optimization problem based on minimizing the Mean Squared Error (MSE) is proposed. Some relaxations are imposed on the original problem (3.5), which is non-convex, to ensure a feasible solution. While the optimization problem (3.8) yields the best estimator in the Minimum Mean Squared Error (MMSE) sense, it poses a memory challenge for large imaging areas. To address this, a suboptimal formulation (3.11) is proposed, which maximizes the trace of the Fisher Information Matrix instead of minimizing the MSE. The solution involves finding the eigenvector corresponding to the largest eigenvalue of matrix $\mathbf{Re}[\mathbf{A}_{tr}]$ as the optimized encoding matrix. Only the real part of the matrix \mathbf{A}_{tr} is considered since we consider amplitude encoding and bi-phase encoding. Despite being suboptimal, this method is more efficient and can provide freedom to focus on a subset of the imaging area for encoding matrix optimization, reducing computational time and increasing flexibility. We determine the focus area through trial and error to find a subset that gives a good imaging result for the overall region. We find out that focusing on the far field area results in a better overall image than focusing on the near field area. The process of selecting a subset of the imaging area is however not discussed and analyzed in detail in this thesis due to time limit.

Additionally, since the thesis focuses on enhancing the image quality of Doppler ultrasound imaging, the case of multiple transmissions to obtain a high-resolution and high-contrast compounded image is considered. A leading eigenvectors transmission scheme is proposed based on the suboptimal formulation. This scheme capitalizes on the fact that matrix $\mathbf{Re}[\mathbf{A}_{tr}]$ in (3.11) has multiple leading eigenvalues that are close to each other which means there might exist multiple optimal solutions. Simulation results also showed that transmitting only the largest eigenvector does not yield satisfactory compounded image quality.

The proposed optimized code transmission scheme is validated through simulations in K-Wave and compared the imaging performance between the optimized code, Barker

code, single short pulse, and random code. Note that the comparisons between different encoding methods are done after normalizing the transmitting energy of all codes so that they have the same average energy. Simulations are done in both small and large array settings. These two settings represent an above-Nyquist sampling frequency array and a sub-Nyquist sampling frequency array, respectively. For the small array where the element pitch-to-wavelength ratio is less than 0.5, the optimized code demonstrates improved SNR in the deeper regions compared to the Barker code, single pulse planewave transmission, and random code, with the same average transmit energy. However, the trade-off is a degradation in axial resolution. This is due to the limitation in the optimization function (3.11), where no constraint of the autocorrelation property of the code is imposed. Conversely, for the large array where the element pitch-to-wavelength ratio is close to 1, the proposed method is not suitable due to limitations in beam steering mobility, making focusing on a specific image area challenging. In this setting, a planewave beam pattern is more appropriate, providing uniform coverage of the imaging area. Simulations in these two settings demonstrate that the optimized code is applicable to the array operating at Nyquist sampling frequency and can outperform other conventional coded excitation schemes considered in this thesis.

Furthermore, the proposed optimized encoding matrix is tested on the clinical M5Sc-D phased array transducer in section 4.3, which operates at the Nyquist sampling frequency. The simulation results align with the small array setting, showing SNR improvements in deeper imaging areas. The optimized code has an SNR gain of 4.4 dB compared to the single short pulse. However, similar trade-offs of reduced axial resolution and a smaller field of view in the near field are observed. The decrease in resolution arises from the limitation of the optimization algorithm, which focuses on maximizing information in the Region of Interest (ROI) but does not account for the autocorrelation property of the code itself. The field of view reduction is attributed to the focused nature of the optimized code since we chose a subset from 50 to 90 mm imaging area to focus on. To address the resolution issue, the iterative least-square technique called LSQR is employed. Results showed that LSQR can drastically improve the resolution of the optimized code with a slight decrease in SNR.

In this thesis, for most cases, we designed an optimized code with a bit-length of 5 due to computational complexity. Theoretically, under the FDA safety limit, the longer the bit-length, the more SNR gain can be expected. A performance comparison between 3-bit, 5-bit, and 10-bit optimized code is conducted and the results show that as bit-length increases, the SNR also increases. The 10-bit code has a GSNR = 3 dB compared to the 3-bit code. However, the resolution decreases as the bit-length increases.

Finally, blood flow simulations are done in the clinical M5Sc-D phased array transducer setting, and the performance between the optimized code and the Barker code is compared. The Doppler imaging results with different additive white Gaussian noise levels, ranging from 0 to -30 dB are shown. Visually, optimized code gives smoother edges on the blood vessels and has a higher intensity in the blood vessel compared to Barker code. Qualitatively, the optimized code exhibits consistent and higher SNR and CNR throughout different noise levels.

5.1 Future Work

Despite the detailed modeling and simulations given in this report, there are still some aspects and possibilities not covered in this thesis. Here, some future work and potential improvements are presented.

1. This thesis has proposed an optimization formulation that is optimal in the MMSE sense. However, its computational complexity poses a challenge for implementation. Future work should focus on developing more efficient algorithms to decrease the computational complexity of the optimization problem (3.8). The solution yielded from (3.8) should expect more improvement in imaging qualities compared to the suboptimal solution implemented in this thesis.
2. Another computational complexity problem arises from the beamforming process of optimized code transmission. Since the transmit pulse from each element differs from each other, the fast DAS beamforming technique cannot be applied to the received ultrasound data \mathbf{y} to form an image. In this thesis, model-based beamforming in the Fourier domain is used, and the construction of model matrix $\mathbf{G}(\mathbf{C})$ is of high complexity. One way to address this problem is to design a decoding matrix based on the optimized encoding matrix. The decoding matrix can then be used to decode the received data \mathbf{y} and geometric focusing, such as DAS can then be applied to form an image. However, the complexity of designing the decoding matrix should also be considered. A similar discussion can be found in the paper [43].

Another way to address this problem is by utilizing compressive sensing techniques, which can significantly reduce computational complexity.

3. In addition to the complexity reduction, future research should also take multi-phase encoding into account. In this thesis, only the bi-phase encoding is considered out of simplicity. Incorporating multi-phase should be able to enhance the performance of the proposed optimized code. Another consideration can be adding phase delays to each phase code in the encoding matrix \mathbf{C} . With phase delays, we can better capture the characteristics of transmitting waveform, for example, a focused beam or a planewave with an angle. This additional consideration will improve the focusing and steering ability of the optimized transmission, leading to further improvements in imaging quality.
4. In this thesis, amplitude encoding is also considered. However, the benefit of amplitude encoding in Doppler ultrasound imaging is not yet clear and needs further investigation. Future work can include dropping the amplitude encoding but only considering the bi-phase encoding, and comparing the performance between amplitude and bi-phase encoding with only bi-phase encoding to see which one yields a better result. A binary constraint then needs to be added to the original optimization function,

$$\begin{aligned} \min \quad & f(\mathbf{C}) \\ \text{s.t.} \quad & \mathbf{c} \in \{-1, 1\}^{NK}. \end{aligned} \tag{5.1}$$

To solve this problem, more sophisticated relaxation techniques should be applied. Another advantage of designing only bi-phase encoding matrices is that when testing and implementing the optimized encoding matrix in the Verasonics system, it will be much easier and more direct since the Verasonics system only supports tri-level transmission. For the amplitude and bi-phase encoding matrix designed in this thesis, before we test it on the Verasonics system, an approximation of its tri-level sequence needs to be done first, which might introduce some errors to the system.

5. The trade-off between SNR improvement and resolution degradation observed for the optimized code in this thesis suggests the need for a more comprehensive trade-off analysis. Future work could investigate optimization strategies to achieve a balanced enhancement of image quality across different imaging parameters. For example, adding an autocorrelation property constraint to the existing optimization function (3.8) and (3.11) to improve the resolution.
6. Conduct Phantom and in vivo experiments on the Verasonic system to test the proposed optimized code on real Doppler data. In this thesis, due to the time limitation, only simulation experiments were conducted. Further experiments on flow phantom using the Verasonic system are important to validate the proposed method and test its applicability.

Conclusions

This research has addressed the challenges encountered in Doppler ultrasound imaging of cerebral blood flow, particularly related to a low SNR and a broad dynamic range in the received signal. It investigated and designed optimized transmit codes for Doppler ultrasound imaging, focusing on increasing SNR. By addressing this problem, this study improved conventional coded excitation schemes and contributed to the gap in optimized code design in ultrasound studies. The proposed novel coded excitation scheme, represented by an encoding matrix, demonstrated significant promise in outperforming established methods like Barker code while utilizing the same number of transmissions and bit-length.

The research commenced with the formulation of a linear signal model incorporating the encoding matrix, followed by the exploration of various imaging techniques to effectively solve this model. A trace-constraint optimization formulation based on maximizing the Fisher information matrix was introduced to find the optimized encoding matrix. Additionally, for scenarios involving multiple transmissions, a leading eigenvectors transmission scheme was proposed and evaluated through extensive simulations, encompassing both small and large array settings.

The simulation results showed that the optimized code exhibited superior SNR in deeper brain regions within the small array setting, compared to conventional methods. However, it was noted that this improvement came with a trade-off in reduced axial resolution, which stems from the limitation in the optimization algorithm. Nevertheless, the application of the iterative imaging technique LSQR proved effective in mitigating the resolution degradation, offering a practical approach to improve image quality.

Finally, a blood flow simulation is done with a clinical M5Sc-D probe setting and the results showed that the optimized code has consistently higher SNR and CNR compared to the Barker code over different noise levels.

The outcomes of this research hold considerable promise for advancing Doppler ultrasound imaging in cerebral blood flow assessment. By enhancing SNR in deeper image regions, the proposed optimized encoding matrix may enable more accurate and informative clinical assessments.

Bibliography

- [1] P. Kruizinga, P. van der Meulen, A. Fedjajevs, F. Mastik, G. Springeling, N. de Jong, J. G. Bosch, and G. Leus, “Compressive 3d ultrasound imaging using a single sensor,” *Science Advances*, vol. 3, no. 12, p. e1701423, 2017.
- [2] E. Mace, G. Montaldo, B.-F. Osmanski, I. Cohen, M. Fink, and M. Tanter, “Functional ultrasound imaging of the brain: theory and basic principles,” *IEEE transactions on ultrasonics, ferroelectrics, and frequency control*, vol. 60, no. 3, pp. 492–506, 2013.
- [3] R. Aaslid, T.-M. Markwalder, and H. Nornes, “Noninvasive transcranial doppler ultrasound recording of flow velocity in basal cerebral arteries,” *Journal of neurosurgery*, vol. 57, no. 6, pp. 769–774, 1982.
- [4] A. A. M. Sivgoulis, G., “Advances in transcranial doppler ultrasonography,” *Current Neurology and Neuroscience Reports*, vol. 9, pp. 46–54, 2009.
- [5] A. A. Sloan MA, “Assessment: transcranial doppler ultrasonography: report of the therapeutics and technology assessment subcommittee of the american academy of neurology,” *Neurology*, vol. 62, no. 9, pp. 1468–1481, 2004.
- [6] S. Golemati, A. Gastounioti, and K. S. Nikita, “Toward novel noninvasive and low-cost markers for predicting strokes in asymptomatic carotid atherosclerosis: The role of ultrasound image analysis,” *IEEE Transactions on Biomedical Engineering*, vol. 60, no. 3, pp. 652–658, 2013.
- [7] B. P. Cox B, “Imaging techniques: Super-resolution ultrasound,” *Nature*, vol. 527, pp. 451–452, 2015.
- [8] E. Tiran, T. Deffieux, M. Correia, D. Maresca, B.-F. Osmanski, L.-A. Sieu, A. Bergel, I. Cohen, M. Pernot, and M. Tanter, “Multiplane wave imaging increases signal-to-noise ratio in ultrafast ultrasound imaging,” *Physics in medicine and biology*, vol. 60, pp. 8549–8566, 10 2015.
- [9] T. Misaridis and J. A. Jensen, “Use of modulated excitation signals in medical ultrasound. part I: Basic concepts and expected benefits,” *IEEE transactions on ultrasonics, ferroelectrics, and frequency control*, vol. 52, no. 2, pp. 177–191, 2005.
- [10] T. Misaridis and J. A. Jensen, “Use of modulated excitation signals in medical ultrasound. part II: Design and performance for medical imaging applications,” *IEEE transactions on ultrasonics, ferroelectrics, and frequency control*, vol. 52, no. 2, pp. 192–207, 2005.
- [11] T. Misaridis and J. A. Jensen, “Use of modulated excitation signals in medical ultrasound. part III: High frame rate imaging,” *IEEE transactions on ultrasonics, ferroelectrics, and frequency control*, vol. 52, no. 2, pp. 208–219, 2005.

- [12] H. Zhao, L. Y. L. Mo, and S. Gao, “Barker-coded ultrasound color flow imaging: theoretical and practical design considerations,” *IEEE Transactions on Ultrasonics, Ferroelectrics, and Frequency Control*, vol. 54, no. 2, pp. 319–331, 2007.
- [13] Food, D. Administration, *et al.*, “Guidance for industry and fda staff information for manufacturers seeking marketing clearance of diagnostic ultrasound systems and transducers,” *Rockville, MD: FDA*, 2008.
- [14] Z. Fan, J. Rudlin, G. Asfis, and H. Meng, “Convolution of barker and golay codes for low voltage ultrasonic testing,” *Technologies*, vol. 7, no. 4, p. 72, 2019.
- [15] Y. M. Benane, D. Bujoreanu, C. Cachard, B. Nicolas, and O. Basset, “An enhanced chirp modulated golay code for ultrasound diverging wave compounding,” in *2018 26th European Signal Processing Conference (EUSIPCO)*, pp. 81–85, IEEE, 2018.
- [16] E. P. Vienneau and B. C. Byram, “A coded excitation framework for increased signal-to-noise ratio of in vivo ultrasound power doppler imaging,” *Proceedings Volume 11602, Medical Imaging 2021: Ultrasonic Imaging and Tomography; 116020P (2021)*.
- [17] E. Grossi, M. Lops, L. Venturino, and A. M. Tulino, “Robust waveform design for mimo radars,” in *2010 IEEE International Symposium on Information Theory*, pp. 1633–1637, 2010.
- [18] H. Xu, J. Zhang, W. Liu, S. Wang, and C. Li, “High-resolution radar waveform design based on target information maximization,” *IEEE Transactions on Aerospace and Electronic Systems*, vol. 56, no. 5, pp. 3577–3587, 2020.
- [19] J. Rubin and R. Adler, “Power doppler expands standard color capability.,” *Diagnostic imaging*, vol. 15, no. 12, pp. 66–69, 1993.
- [20] J. Bercoff, G. Montaldo, T. Loupas, D. Savery, F. Mézière, M. Fink, and M. Tanter, “Ultrafast compound doppler imaging: Providing full blood flow characterization,” *IEEE transactions on ultrasonics, ferroelectrics, and frequency control*, vol. 58, no. 1, pp. 134–147, 2011.
- [21] V. Perrot, M. Polichetti, F. Varray, and D. Garcia, “So you think you can das? a viewpoint on delay-and-sum beamforming,” *Ultrasonics*, vol. 111, p. 106309, 2021.
- [22] R. Lavarello, F. Kamalabadi, and W. O’Brien, “A regularized inverse approach to ultrasonic pulse-echo imaging,” *IEEE Transactions on Medical Imaging*, vol. 25, no. 6, pp. 712–722, 2006.
- [23] C. Demené, T. Deffieux, M. Pernot, B.-F. Osmanski, V. Biran, J.-L. Gennisson, L.-A. Sieu, and Bergel, “Spatiotemporal clutter filtering of ultrafast ultrasound data highly increases doppler and fultrasound sensitivity,” *IEEE Transactions on Medical Imaging*, vol. 34, no. 11, pp. 2271–2285, 2015.
- [24] M. L. Thorne, R. N. Rankin, and Steinman, “In vivo doppler ultrasound quantification of turbulence intensity using a high-pass frequency filter method,” *Ultrasound in medicine & biology*, vol. 36, no. 5, pp. 761–771, 2010.

- [25] R. Y. Chiao and X. Hao, “Coded excitation for diagnostic ultrasound: A system developer’s perspective,” *IEEE transactions on ultrasonics, ferroelectrics, and frequency control*, vol. 52, no. 2, pp. 160–170, 2005.
- [26] I. Trots, “Mutually orthogonal golay complementary sequences in synthetic aperture imaging systems,” *Archives of Acoustics*, vol. 40, no. 2, pp. 283–289, 2015.
- [27] P. Ni and H.-N. Lee, “High-resolution ultrasound imaging using random interference,” *IEEE Transactions on ultrasonics, ferroelectrics, and frequency control*, vol. 67, no. 9, pp. 1785–1799, 2020.
- [28] M. A. Richards, J. Scheer, W. A. Holm, and W. L. Melvin, *Principles of modern radar*. Citeseer, 2010.
- [29] J. T. Fokkema and P. M. van den Berg, *Seismic applications of acoustic reciprocity*. Elsevier, 1993.
- [30] S. M. Kay, *Fundamentals of Statistical Signal Processing: Estimation Theory*. Prentice Hall, 1997.
- [31] C. R. Vogel, *Computational Methods for Inverse Problems*. Society for Industrial and Applied Mathematics, 2002.
- [32] P. van der Meulen, P. Kruizinga, J. G. Bosch, and G. Leus, “Coding mask design for single sensor ultrasound imaging,” *IEEE Transactions on Computational Imaging*, vol. 6, pp. 358–373, 2019.
- [33] S. P. Chepuri, “Sparse sensing for statistical inference: Theory, algorithms, and applications,” 2016.
- [34] T. Schonhoff and A. Giordano, *Detection and Estimation Theory and Its Applications*. PearsonPrentice Hall, 2006.
- [35] S. Boyd and L. Vandenberghe, “Semidefinite programming relaxations of non-convex problems in control and combinatorial optimization,” *Communications, Computation, Control, and Signal Processing: a tribute to Thomas Kailath*, pp. 279–287, 1997.
- [36] E. Feron, “Nonconvex quadratic programming, semidefinite relaxations and randomization algorithms in information and decision systems,” *System Theory: Modeling, Analysis and Control*, pp. 255–274, 2000.
- [37] Z.-Q. Luo, W.-K. Ma, A. M.-C. So, Y. Ye, and S. Zhang, “Semidefinite relaxation of quadratic optimization problems,” *IEEE Signal Processing Magazine*, vol. 27, no. 3, pp. 20–34, 2010.
- [38] M. Grant, S. Boyd, and Y. Ye, “Cvx: Matlab software for disciplined convex programming,” 2009.
- [39] S. P. Boyd and L. Vandenberghe, *Convex optimization*. Cambridge university press, 2004.

- [40] B. E. Treeby and B. T. Cox, “k-wave: Matlab toolbox for the simulation and reconstruction of photoacoustic wave fields,” *Journal of biomedical optics*, vol. 15, no. 2, pp. 021314–021314, 2010.
- [41] T. Szabo, *Diagnostic Ultrasound Imaging: Inside Out*. Biomedical Engineering, Elsevier Science, 2013.
- [42] M. A. S. Christopher C. Paige, “Lsqr: An algorithm for sparse linear equations and sparse least squares,” *ACM Transactions on Mathematical Software*, vol. 8, no. 1, pp. 43–71, 1982.
- [43] N. Bottenus, J. Spainhour, and S. Becker, “Comparison of spatial encodings for ultrasound imaging,” *IEEE Transactions on Ultrasonics, Ferroelectrics, and Frequency Control*, vol. 70, no. 1, pp. 52–63, 2022.